SLAC–PUB–5793
April 1992
(I)

Wire Chamber Gases*

J. Va'vra

Stanford Linear Accelerator Center, Stanford University, Stanford, CA 94309, USA

Abstract

In this paper, we describe new developments in gas mixtures which have occurred during the last 3–4 years. In particular, we discuss new results on the measurement and modeling of electron drift parameters, the modeling of drift chamber resolution, measurements of primary ionization and the choice of gas for applications such as tracking, single electron detection, X-ray detection and visual imaging. In addition, new results are presented on photon feedback, breakdown and wire aging.

Invited talk presented at the Wire Chamber Conference, Vienna, Austria, February 17–21, 1992.

* Work supported by Department of Energy contract DE–AC03–76SF00515.

1. Introduction

We have selected several examples from the vast subject of wire chamber gases to illustrate the progress which has been made during the last several years. For example, there has been very important progress in the development of computer codes to simulate electron transport parameters with precision adequate for most applications; also, there is better understanding of breakdown problems and associated photon feedback, there are now various choices of photocathodes for CRID/RICH detectors, and the properties of helium and CF_4-based gas mixtures, which are useful gases for many applications at SSC/LHC, Phi, Tau-Charm, and B factories, are much better understood.

2. Measurements and modeling of the electron drift parameters

Real progress has been made in this subject in the last several years, in both the theoretical and experimental areas.

In this paper, we mention the results of calculations of electron transport parameters based on four models; these are the calculation due to Ness and Robson [1], the MAGBOLTZ code of Biagi [2,3], the WIRCHA code of Fehlmann [4], and the calculation of Frazer and Mathieson [5]. They are all based on solutions of the Boltzmann equation with various degrees of complexity. A multiterm solution of the Boltzmann equation, due to Ness and Robson [1] is the most sophisticated at the moment, since it includes anisotropic elastic scattering formalism and a general parametrization of the magnetic field due to Ness, which does seem to agree with data [6]. However, we found [7] that Biagi's second order solution works very well in many applications, and has one advantage at present,

since it includes ionization and attachment effects, and furthermore is readily available.

Fig. 1 shows the CH_4 gas drift velocity and diffusion data of Schmidt [8] in comparison with a calculation of Ness [6]. In order to obtain such excellent agreement with the data it was necessary to include anisotropic elastic scattering cross sections and to carry out the multiterm expansion to order $l = 6$. In addition, the authors measured drift velocity, as well as longitudinal and transverse diffusion in many molecular gases and mixtures based on helium, argon, neon, krypton, xenon and CF_4 gases [6]. The aim was to extract electron scattering cross sections and test the theory. They have also undertaken a comprehensive program to measure drift parameters in magnetic field [6].

Va'vra et al. [7] measured many helium and CF_4-based gas mixtures and compared data with available models [2–5]. Figs. 2–6 show the results. A conclusion was that among the tested models, the Biagi calculation [2,3] agrees best with the data. However, there are still some disagreements, for example in the case of CF_4 gas (see fig. 6). Difficulties of the simulation codes with CF_4 gas may be linked to a considerable disagreement among existing measurements, especially at high E/p (see fig. 7). Similar problems exist at present with He + DME mixtures [7].

It is not an easy task to measure the electron transport parameters if one wants to constrain the models meaningfully. One has to pay very careful attention to systematic effects resulting from gas mixture calibration, TDC calibration, gas impurity, H_2O, O_2, temperature and pressure monitoring, mechanical errors, etc. To quote a few examples of the precision achieved, Christophorou et al. [9] quote errors in drift velocity at the 5–7% level, Dolgoshein et al. [10] at the 5% level for drift velocity, Schmidt [11] achieved 1% accuracy for drift velocity and 5% accuracy for single electron transverse and longitudinal diffusion, while

Va'vra et al. [7] quote 3% uncertainty for the drift velocity and 5–10% uncertainty for single electron longitudinal diffusion.

3. Modeling of drift chamber resolution

To illustrate the progress in this area, we discuss an attempt to incorporate the improvements in the modeling of the electron transport parameters mentioned in the previous chapter into a simulation of spatial resolution in an actual geometry; this includes the proper simulation of the electrostatics, the primary ionization deposits, electron drift, avalanche fluctuations, electronics, etc. This was done recently by Biagi [3], and we will mention his results later in chap. 6 when we discuss problems with CF_4 tracking.

4. Primary ionization

The new results include measurement of the number of primary clusters and measurement of the electron multiplicity distribution within these clusters.

Pansky et al. [12] reported a measurement of the primary cluster ionization as a function of various gases, including TEA and TMAE. The measurement was done using a low pressure technique. Table 1 shows their results together with older data of Rieke and Prepejchal [13] obtained with a streamer chamber technique. The very large ionization yield in case of TMAE should be noted.

Fischle et al. [14] measured the distribution of electron multiplicity within the primary ionization clusters in Ar, CH_4, He, CO_2, C_2H_6, C_3H_8 and iC_4H_{10} gases. The ingenious technique to extract the primary clusters from a β track (Sr^{90} source) is described in fig. 8. The extracted clusters were then allowed to spread at low pressure (100 Torr) and low drift field (10 V/cm) to allow their individual

detection. It was very important to have very efficient detection of single electrons, even for very small pulses near pedestal. In order to limit possible background due to secondary avalanche effects, they used very thick anode wires (400 and 800 μm diameter). An example of their results is shown in fig. 9 for argon gas. They found that all of the previously mentioned hydrocarbon molecules have almost the same electron distribution within the clusters, and that very light elements contain a larger proportion of single electron clusters than do more complex atoms [$p(1)_{methane} = 0.79$ and $p(1)_{argon} = 0.66$, where p(1) is a probability of having a single electron cluster]. The data do not seem to agree with the calculation of Lapique and Piuz [15], which is based on the photo-absorption model of Chechin et al. [16] [data: $p(1)_{argon} = 0.656 \pm 0.016$, model: $p(1)_{argon} = 0.802$; also the data do not support a predicted bump at n =10 due to L absorption edge of argon].

Since there has been considerable interest in helium-based gases recently, it should be mentioned that such mixtures have a strong Penning effect because He^* metastable levels have high energy (19.8 and 20.6 eV). A few parts in 10000 of almost any admixture present in helium will increase the ionization yield by about 40–50% [17]. An addition of Neon gas does not have such an effect due to its high ionization potential of 21 eV.

5. Photon feedback and breakdowns

Progress in this area is represented in a better understanding of the breakdown and associated photon feedback processes.

Let us start with **a general description of photon production during an avalanche process.** Early studies indicated that the mechanism was highly com-

plex. For instance, Peskov [18] and Charpak et al. [19] measured emission photon spectra as a function of many conditions: geometry, charge gain, gas, pressure, etc. Fig. 10(a) indicates what appears to be a rather complex dependence on pressure, while fig. 10(b) shows that the photon per avalanche charge yield is peaking at lower charge yields. Subsequently people found many simplifying features. For example, Sauvage et al. [20] observed a simple linear correlation between charge and light yields in 70% C_2H_6 + 30% Ar + TMAE at 100 Torr using a phototube to detect light and a parallel plate chamber (PPAC) to detect charge (see fig. 11). More recently, Fonte et al. [21] found that the photon yield in Ar + TEA, He + TEA, Ar + CH_4, He + CH_4 and Ar + C_2H_6 gases operating in the PPAC at low pressure between 120–170 nm can be described using laws involving a "photon-equivalent" first Townsend coefficient similar to the charge yield, i.e., the ionization and photon excitations seem to obey similar laws in this respect ($\delta/p = A.e^{-Bp^k/E}$, where δ is the "photon-equivalent" first Townsend coefficient, E is the electric field, p is partial pressure of the quencher gas and k is the gas constant).

What are the sources of UV photons? Excited atomic levels of carbon C^*(6.43, 7.46 and 7.94 eV), nitrogen N^*(8.3, 10.0 and 10.3 eV) or hydrogen H*(10.2 eV), etc., are usually responsible for photon emission. These elements are typical constituents of gases used in detectors. Hard UV photons are responsible for creation of secondary photoelectrons, either in a photosensitive gas or in nearby electrodes. In practice, this causes secondary hits, increases in pad multiplicity, and, as we will see later, voltage breakdowns.

Let us start with wire chambers. Arnold et al. [23] have studied the Fast RICH with pad readout. By changing additives such as CH_4, C_2H_6 or iC_4H_{10} to a photosensitive gas such as TMAE or TEA, various excitation lines can be eliminated

[see fig. 12(a)]. For instance, with CH_4 + TMAE gas the detector is sensitive to all three C^* excitation lines, with 75% CH_4 + 25% iC_4H_{10} + TMAE gas it is sensitive only to the C^*(6.43 eV) line, while with CH_4 + TEA gas it is sensitive only to the C^*(7.94 eV) and N^*(8.3 eV) lines, etc. A change of the UV photon production rate resulted in a change of a pad multiplicity rate [see fig. 12(b)], and the gas with the smaller photon rate results in more stable detector operation. For example, the MWPC filled with CH_4 + TEA has operated stably with gain up to 2×10^6, whereas with CH_4 + C_2H_6 + TMAE the gain was limited to 6×10^5. To quote another example, fig. 12(c) shows the secondary hit rate due to photon feedback in the CRID detector at SLD [22]. Use of C_2H_6 + TMAE gas makes the detector sensitive to all three C^* excitation lines. The rate of secondary hits is about 1% per primary avalanche, thanks to a blind structure with which these detectors are equipped (without the blinding structure it would be about 7%).

In the PPAC the UV photon sources are similar. Fonte et al. [21] found that in pure argon photon emission is dominated by the Ar_2^* band (120–140 nm). However, with a small addition of hydrocarbons such as TEA, the emission was quickly dominated by the C^* and N^* emission lines, even at a quencher concentration of only a few Torr. Fig. 13 shows the UV photon yield in the 120–180 nm range as a function of TEA quencher partial pressure. The photon yield decreases as a function quencher pressure and varies by several orders of magnitude. What is important in the previous paragraph is that the resulting photoelectron yield, η, depends on the gas used, chamber construction, the Q.E. of surfaces, etc.

The breakdown problem. Let us begin with the PPAC chamber. If G is the total charge gain, N_0 is the deposited ionization charge, and η is the total photoelectron feedback rate, Fonte et al. [21] found experimentally using the PPAC that for the condition $\eta.G > 1$, **"a slow breakdown"** develops; this occurs with ~10 μs

delay, is photon feedback mediated and causes the chamber to become totally inoperable. For the condition $N_0.G > 10^8$, **"a fast breakdown"** develops; this occurs with only tens of ns delay, is space charge mediated and the chamber recovers to full operation quickly. We illustrate these conditions by means of two examples: (a) if $N_0 = 220$ (Fe^{55} source), then $G = 5 \times 10^5$ is the maximum gain before the fast breakdown occurs; (b) if $\eta = 2 \times 10^{-6}$, then slow breakdown will occur at a gain of about $G = 5 \times 10^5$. The fast breakdown limit is consistent with a 40-year-old prediction of Meek and Raether [24,25], which says that the maximum charge gain occurs for $\alpha.d \sim 20$ (d is the gap in the PPAC, α is the first Townsend coefficient and $G = e^{\alpha.d}$). Of course, at that time it was done with completely different gases. Spark formation is independent of the detailed characteristics of the gas; this is because fast breakdown is related to space charge buildup which locally distorts the electric field to the point that very excessive gain is reached. A problem related to the PPAC, especially when used for single electron detection, which requires higher gain operation, is that it is linear in charge yield all the way up to the sparking limit [21]. Such a chamber is prone to sparking in a harsh background environment. On the other hand, a wire chamber **saturates** the charge development, thus impeding the onset of the fast breakdown limit. In this sense, a wire chamber is a safer instrument to use in an environment where one operates in the vicinity of the fast breakdown limit [26]. The PPAC problem can be reduced in some applications by making use of double or triple stage parallel plate chambers [21] which can be gated.

6. Applications

6.1. Tracking

Two very general observations concerning tracking gases are that gases with large dipole moment give slow electron drift velocity, and that gases with large infrared absorption cross section give low diffusion.

The need to reduce event occupancy in straw tube detectors at the SSC/LHC, has lead to considerable interest in radiation hard, **fast** gases based on $\mathbf{CF_4}$. In addition. the need for improved momentum resolution in the central tracking chambers of future Phi, Tau-Charm and B factories has led to the study of **low mass** gases with reduced multiple scattering based on **helium**. Table 2 contains a brief summary of the advantages and disadvantages of these two types of gases.

Playfer et al. [27] simulated helium-based gases with the program WIRCHA [4], and concluded that about 20–30% of quencher is needed in order to achieve low diffusion and reasonable drift velocity (see fig. 14). Schmidt and Martens [28] measured many helium-based gas mixtures and decided to evaluate them with a figure of merit $fm_{L,T} = (\sqrt{2\varepsilon_{L,T}/E}) / (\sqrt{N_p})$, where $\varepsilon_{L,T}$ is the characteristic energy and N_p is the number of primary electrons, as a measure of the final tracking resolution (see fig. 15). They recommend 10–20% of iC_4H_{10} as a candidate for helium-based mixtures used for tracking in the 1 GeV/c region. Va'vra et al. [7] also measured many basic gas parameters (figs. 2–7) and concluded that one should be concerned about secondary avalanche effects in helium-based mixtures; these can be recognized from Polya fits to single electron pulse height spectra. Again, they found that 15–20% of quencher appears to be sufficient. Grab et al. [29] investigated dE/dx performance for mixtures consisting of 80% He +

20% iC_4H_{10}, 80% He + 20% DME and 70% He + 30% DME; they concluded that the *dE/dx* performance should be only 10–20% worse than with standard mixtures such as 50% Ar + 50% C_2H_6. More information on the practical applications of helium-based gases is given in the talk by Boyarski [30].

It is well known that the CF_4 molecule can absorb an electron and dissociate to form F^- and CF_3^- negative ions together with F^*, CF_2^* and CF_3^* radicals. The probability for this process peaks at an electron energy of about 6–7 eV [31,34], i.e., the process occurs only near the wire and can be responsible for a loss of electrons before the avalanche starts. Christophorou et al. [9] found experimentally that CF_4 gas absorbs electrons in an 8–35 kV/cm/atm window, while for 80% Ar + 20% CF_4 the corresponding range is 2–20 kV/cm/atm (note that a gas has good high voltage behavior as long as the effective ionization coefficient $\bar{\alpha}/N = \alpha/N - \eta/N$ is negative [9], where α/N and η/N are the ionization and attachment coefficients, respectively—see fig. 16). However, 80% Ar + 10% CO_2 + 10% CF_4 does not absorb electrons. Presumably, if enough quencher is added to CF_4 gas (e.g., 20% of iC_4H_{10}), electrons are cooled to the extent that attachment does not occur. What are the consequences of electron attachment near the wire? Biagi [3] has shown in his computer simulation of 4 mm diameter straw tubes that if a mixture such as 90% Ar + 10% CF_4 is used, there can be a real deterioration in spatial resolution (see fig. 17). Most of the attachment occurs between 10 and 25 wire diameters from the anode wire, and only 15% of the original electrons reach the anode wire from a distance of 0.9 mm. Additional concerns about CF_4-based gas mixtures in connection with high rate applications are raised by Yamashita et al. [32], who pointed out that the positive ion mobility in CF_4 gas is much lower than, for example, in CH_4 (see fig. 18). Consequently, it was reassuring when the SDC collaboration published [33] good results on rate handling

capability and tracking resolution in a 4 mm diameter straw tube using 80% CF_4 + 20% iC_4H_{10} gas (see fig. 19).

6.2. X-ray detection

Dolgoshein et al. [10] have measured many Xe-based mixtures at 1 atm for TRD application at SSC/LHC (see fig. 20). They found a poor Fe^{55} source resolution of about 60% FWHM for some Xe + CF_4 mixtures due to the dissociative electron capture mentioned above (see fig. 21). Similar results were published by Christophorou for 90% Ar + 10% CF_4 [34]. Because of this effect and because CO_2 is only about half as dense as CF_4 (smaller dE/dx), Dolgoshein et al. prefer Xe + CO_2 mixtures for Transition Radiation (TR) applications.

Breskin et al. [35] investigated X-ray detection using PPAC detectors with C_2H_6, iC_4H_{10} and DME gases at pressures of about 10–40 Torr and solid CsI photocathodes. A very high gain of about 5×10^7 was achieved in DME gas. Such detectors are fast (<1 ns), and are capable of high rate (fast ion removal), low dE/dx deposits with localization accuracy of about 200 μm FWHM. Traditional TR detectors, such as straw tubes with Xe-based gases are slow (<30 ns), and have large dE/dx and delta-ray background.

Finally, the excellent pulse height resolution results obtained with microstrip gas chambers operating with Xe-based gases [36] should be mentioned. Values as low as 10–11% FWHM were achieved with an Fe^{55} source; this is far superior to what can be obtained with MWPC chambers.

For a general overview of X-ray detection, we refer to ref. 37.

6.3. Single electron detection

There is an interest in developing this technique for Fast Cherenkov Ring Imaging (Fast RICH) at the SSC/LHC and B factory accelerators. Fig. 22 shows two possible candidates, one is based on a MWPC with pad readout operating with either CH_4 + TEA gaseous or CsI + TMAE solid photocathodes [23]; the other is based on a single gap PPAC, also with pads, operating with a CsI + TMAE photocathode and iC_4H_{10} gas at 20 Torr pressure [38,39]. Fig. 23 shows the quantum efficiencies for several possible photocathodes [23]. However, as was described in chap. 5 and supported by practical experience [26], it is an open question whether a single gap PPAC used in a single electron detecting mode can survive SSC/LHC backgrounds if they are as bad as in the present heavy ion environment. Similarly, the radiation aging in both applications is still an open question. In addition, the solid photocathodes are probably more sensitive to various plating problems (positively charged avalanche fragments, accidents with gases, etc.). One interesting gaseous photocathode to try is 80% CF_4 + 20% C_4H_{10} + TMAE (60°).

Finally, one should mention a proposal of Giomataris and Charpak [40] for a hadron blind threshold Cherenkov detector. It would use a PPAC operating at 1 atm with He + 3000 PPM of CF_4, with a CsI photocathode, and without any front window. CF_4 gas is more transparent than CH_4, and the hope is to widen the usual "TMAE 1 eV wide band width window" by a few eV in order to increase overall efficiency. However, more experimental work is needed to validate this idea.

6.4. Visual imaging

In chap. 5, we discussed UV photon production in avalanches. However, photons are also produced in the visible and near-visible range in the presence of a suitable additive. For instance, 98% Ar + 2% CH_4 + 0.04% TMAE gas emits between 400 and 600 nm, and 94% Ar + 6% TEA between 260 and 340 nm [41,42]. The PPAC increases the light yield, and allows the use of a thin, wavelength-shifting scintillator placed just before the exit window. The gas mixture with TEA proved to be more stable in applications for visual imaging.

7. Wire aging

Although some progress has been made in the area of simple cookbook rules, and in the understanding of aging due to formation of nonconducting surface films on anode wires [43–45], nevertheless, we still lack a real understanding. Perhaps it should be mentioned that new techniques have been developed for identifying the fragments of avalanches, and some connections between wire aging problems and the plasma chemistry have been identified.

The best advice one can give is to test wire aging in as realistic a setup as possible. This should include a detector with realistic geometry, functioning at its true operating point, the use of gases with planned purity, and the presence of all contaminating materials such as glues, etc. If the wire aging test ends up to be positive under such conditions, one can have some hope for the final application. This is what, for instance, Bondarenko et al. [46] did; they found no aging in their straw tubes for doses up to 1.5 C/cm in gases such as 50% Xe + 50% CO_2 and 50% Xe + 30% CO_2 + 20% CF_4.

If wire aging occurs, some remedy must be found [43–45]. An interesting solution was found by Openshaw et al. [47] in the case of aging in 50% Ar + 50% C_2H_6. They found that the gain can be restored, and deposits on the anode wires removed, by running 80% CF_4 + 20% C_4H_{10} and operating the chamber with a source. It is well known that CF_4 gas is used in industry for etching purposes. This experiment created much interest in using CF_4-based gases for the prevention of aging. However, one should be careful [48] to verify that the actual anode wire is not etched, and thereby reduced in diameter.

Subsequently, it was surprising to learn that CF_4 gas alone was found to age rather significantly [49], as can be seen in fig. 24(a). This was found to be independent of anode wire material and gas purification, including the Nanochem filter [50]. As was stated earlier, the CF_4 molecule can be dissociated easily if drifting electrons exceed 4–5 eV in energy. The iC_4H_{10} admixture will tend to lower the average electron energy in the avalanche, as can be seen in fig. 24(c); therefore it will reduce the probability of negative ion formation. The negative ions will tend to drift towards the anode wire. It is presently unclear why this mechanism will produce a different rate of wire aging between the two above-mentioned CF_4 gases. One possibility is that, in the case of 80% CF_4 + 20% iC_4H_{10}, the isobutane serves as a material on which the fluorine and fluorocarbon radicals react, with the resulting products tending to be volatile [47]. Apparently, this mechanism is absent in the case of CF_4 gas alone, and the anode wire is coated, or reacts to form a nonconducting metallic fluoride [53].

Helium-based gases have been tested thus far only in tube geometries [7], and, as one can see in fig. 24(b), the aging rate is zero or small (this test should be repeated in an open wire geometry to investigate the importance of cathodic effects, such as the Malter effect). The electrons in the 95% He + 5% C_2H_6 gas mix-

ture tend to be much hotter, as one can see in fig. 24(c). Perhaps, they can destroy any polymerization product, and the resulting species are volatile.

We do not have a real understanding of the wire aging process, at least to the extent which physicists would like. We need more quantitative information, such as the average energy of electrons near the wire [see fig. 24(c)], or information about avalanche fragments. One example in the latter category which we would like to mention is the measurement of Fraga et al. [51]; they measured light production in the region from 120 to 400 nm in order to identify the presence of ions and radicals [see fig. 25(a),(b)]. The advantage of this technique is that it identifies the fragments at the moment of creation. On the other hand the limitation is that it sees only "bright" fragments, and might miss "dim" ones. Another example worth of mentioning is the GC-MS analysis of avalanche products [53,54]. To enhance the signal in this case, it was necessary to cryotrap the avalanche byproducts after they left a test tube chamber. This means that only final stable and heavier molecules were seen. Fig. 26(a),(b) shows their results. What is interesting is that 50% Ar + 50% C_2H_6 and CF_4 gases behave completely differently. When high voltage on the chamber is on, and source is active, the former gas produces a large amount of hydrocarbon fragments in the avalanche, whereas CF_4 gas yields very little. However, as soon as the source is removed, CF_4 gas yields a large number of molecules, as can be seen in fig. 26(b). In other words, the chamber traps CF_4-based molecular fragments during operation with a source, as if most of the fragments were negatively charged and trapped by the anode wire. This is not understood at the moment, but the almost "digital" character of the process gives some hope for underlying simplicity.

8. Conclusions

It is clear that the physics of gases and surface phenomena is such a rich and complex subject as to ensure that the Vienna Conference has good prospects well into the next century!

Acknowledgements

We thank Dr. S. Biagi for providing his electron transport calculations for various gases discussed in this paper. We also thank Drs. G. Viertel and H. Anderhub for running the WIRCHA program for us.

References

[1] K. F. Ness and R. E. Robson, Phys. Rev. A, 38 (1988) 1446.

[2] S. Biagi, Nucl. Instr. & Meth. A283 (1989) 716.

[3] S. Biagi, Nucl. Instr. & Meth. A310 (1991) 133.

[4] J. Fehlmann, J. Paradiso, and G. Viertel, WIRCHA Simulation program, ETH Zurich, March 1983 and J. Fehlmann, Ph.D. thesis No. 8711, ETH Zurich, 1988.

[5] G. W. Fraser and E. Mathieson, Nucl. Instr. & Meth. A257 (1987) 339.

[6] K. Berkhan, B. Gotz, T. Kunst, K. Ness, and B. Schmidt, Proc. Wire Chamber Conf., Vienna, Austria, 1992.

[7] J. Va'vra, P. Coyle, J. Kadyk, and J. Wise, SLAC–PUB–5728 (1992).

[8] B. Schmidt, Journal of Physics B, 24 (1991) 4809.

[9] P. G. Datskos, J. G. Carter, and L. G. Christophorou, J. Appl. Phys. 71 (1992) 15.

[10] B. Dolgoshein et al., CERN–EP–89–16.

[11] B. Schmidt, Nucl. Instr. & Meth. A273 (2988) 488.

[12] A. Pansky, G. Malamud, A. Breskin, and R. Chechik, Proc. Wire Chamber Conf., Vienna, Austria, 1992.

[13] F. F. Rieke and W. Prepejchal, Phys. Rev. A6 (1972) 1507.

[14] H. Fischle, J. Heintze, and B. Schmidt, HD–PY–90/04.

[15] F. Lapique and F. Piuz, Nucl. Instr. & Meth., 175 (1980) 297.

[16] V. A. Chechin et al., Nucl. Instr. & Meth., 98 (1972) 577.

[17] W. P. Jesse and J. Sadauskis, Phys. Rev. 100 (1955) 1735.

[18] V. D. Peskov, J. Applied Spectroscopy (USSR) 30 (1979) 860.

[19] G. Charpak et al., Nucl. Instr. & Meth. A269 (1988) 142.

[20] D. Sauvage, A. Breskin, and R. Chechik, Nucl. Instr. & Meth. A275 (1989) 351.

[21] P. Fonte, V. Peskov, and F. Sauli, Nucl. Instr. & Meth. A305 (1991) 91.

[22] K. Abe et al., SLAC–PUB–5214 (1990).

[23] R. Arnold, Y. Giomataris, J. L. Guyonnet, A. Racz, J. Seguinot, and T. Ypsilantis, CERN–LAA/PI/91–014.

[24] H. Raether, Z. Phys. 112 (1939) 464.

[25] J. M. Meek, Phys. Rev. 57 (1940) 722.

[26] H. J. Specht, Proc. Wire Chamber Conf., Vienna, Austria, 1992.

[27] S. M. Playfer et al., ETHZ–IMP–PR–01–3 (1991).

[28] B. Schmidt and K. Martens, J. of Physics B, 24 (1991) 4809.

[29] C. Grab et al., ETHZ–IMP, pp. 92–3, 1992.

[30] A. Boyarski, D. Briggs, and P. Burchat, Proc. Wire Chamber Conf., Vienna, Austria, 1992.

[31] P. W. Harland and J. C. J. Thynne, Int. J. Mass Spectr. Ion Phys. 9 (1972) 253; K. A. G. MacNeil and J. C. J. Thynne, Int. J. Mass Spectr. Ion Phys. 3 (1970) 455.

[32] T. Yamashita et al., Nucl. Instr. & Meth. A283 (1989) 709.

[33] Conceptual design report, SDC–91–00125.

[34] L. G. Christophorou et al., Nucl. Instr. & Meth., 163 (1979) 141.

[35] A. Breskin, S. Majewski et al., Nucl. Instr. & Meth. A310 (1991) 57.

[36] F. Angelini, R. Bellazzini, A. Brez, M. M. Massai, L. Shektman, G. Spandre, Proc. Wire Chamber Conf., Vienna, Austria, 1992.

[37] C. Budtz-Jorgensen, Rev. Sci. Instrum. 63 (1992) 648.

[38] Many people contributed to the development of the PPAC; G. Charpak, V. Peskov, F. Sauli, A. Breskin, H. Specht and D. Anderson, to name but a few.

[39] S. Kwan and D. F. Anderson, Nucl. Instr. & Meth. A309 (1991) 190.

[40] Y. Giomataris and G. Charpak, Nucl. Instr. & Meth. A310 (1991) 589 and Proc. Wire Chamber Conf., Vienna, Austria, 1992.

[41] G. Charpak, Nucl. Instr. & Meth. A310 (1991) 47.

[42] F. Sauli, invited talk, Proc. Wire Chamber Conf., Vienna, Austria, 1992.

[43] Proc. Workshop on Radiation Damage to Wire Chambers, LBL, Berkeley, CA, LBL–21270 (1986), J. A. Kadyk, editor.

[44] J. Va'vra, Nucl. Instr. & Meth. A252 (1986) 547 and SLAC–PUB–5207 (1990).

[45] J. A. Kadyk, Nucl. Instr. & Meth. A300 (1991) 436.

[46] V. G. Bondarenko et al., CERN–PPE/91–191.

[47] R. Openshaw et al., Nucl. Instr. & Meth. A307 (1991) 298.

[48] B. Schmidt, private communication at Wire Chamber Conf., Vienna, Austria, 1992.

[49] J. Wise, J. A. Kadyk, and D. W. Hess, Proc. Wire Chamber Conf., Vienna, Austria, 1992.

[50] Nanochem Model L–60, Semi-gas System Inc., San Jose, CA 95126, USA.

[51] M. Fraga et al., Proc. Wire Chamber Conf., Vienna, Austria, 1992.

[52] Prof. Policarpo, private communication.

[53] J. Wise and J. A. Kadyk, Nucl. Instr. & Meth. A300 (1991) 436.

[54] J. Wise, Ph.D. thesis, LBL (1992).

[55] R. A. Holroyd, J. M. Preses, C. L. Woody, and R. A. Johnson, Nucl. Instr. & Meth. A261 (1987) 446.

[56] S. Ekelin, Internal Report, Royal Institute of Technology, Stockholm (1981).

Figure Captions

1. A comparison of data [8] and calculation [1] for (a) drift velocity and (b) diffusion coefficient in CH_4 gas.

2. (a) The electron drift velocity in 50% Ar + 50% C_2H_6. The dot-dash curve is a calculation of Biagi [2,3].

   (b) Single electron longitudinal diffusion in the same gas; the solid curve is a the $1/(\sqrt{E})$ dependence, the dot-dash curve is a calculation of Biagi [2,3], the dashed curve is the calculation of Fraser and Mathieson [5], and the dotted curve is the prediction of the WIRCHA program [4].

3. (a) The drift velocity in 78% He + 15% CO_2 + 7% iC_4H_{10} gas [7]; the solid curve is to guide the eye, the dot-dash curve is a calculation of Biagi [2,3].

   (b) Single electron longitudinal diffusion in the same gas [7]. The dot-dash curve is a calculation of Biagi [2,3], the dotted curves are predictions from the WIRCHA program [4], the solid curve is a $1/(\sqrt{E})$ fit to the data.

4. (a) Electron drift velocity in 95% He + 5% C_2H_6 and 50% He + 50% C_2H_6 gases [7]; the solid curve is to guide the eye, the dot-dash curve is a calculation of Biagi [2,3].

   (b) Single electron longitudinal diffusion in the same gases [7]; the dot-dash curve is a calculation of Biagi [2,3], the dotted curves are predictions of the WIRCHA program [4].

5. (a) Electron drift velocity in the DME gas [7]; the dot-dash curves are calculations of Biagi [2,3].

   (b) Single electron longitudinal diffusion in the same gas; the dot-dash curves are calculations of Biagi [2,3].

6. (a) Electron drift velocity in the CF4-based gases [7]. The dot-dash curve is a calculation of Biagi [2,3].

   (b) Single electron longitudinal diffusion in the same gases [7]; the solid curves are $1/(\sqrt{E})$ fits, the dot-dash curve is a calculation of Biagi [2,3].

7. (a) CF_4 electron drift velocity data.

   (b) The same at higher drift field.

8. A detailed view of the cluster extraction device [14].

9. The experimental results on cluster size distribution for argon gas [14], and the results for the model of Lapique and Piuz [15].

10. (a) The photon emission spectrum from argon excited by an avalanche [18]; 100 μm wire diameter, gain 100, Fe^{55} source, pressure 0.1 atm (1), 1 atm (2), 10 atm (3) and 25 atm (4).

    (b) Photon emission normalized to avalanche charge as a function of avalanche charge for 98% Ar + 2% TEA (1), Ar + TMAE (0.4 Torr) (2), 87% He + 11% CH_4 + 2% TEA (3), 97% Ar + 3% CH_4 + TMAE (0.4 Torr) (4) and CH_4 + TMAE (0.4 Torr) (5) [19].

11. The correlation between light and charge production in avalanches in a PPAC operating with 70% C_2H_6 + 30% Ar + 3% TMAE at 100 Torr with a Fe^{55} source [20].

12. (a) The relative position of C^* and N^* photon emission lines within the photosensitive window defined by TMAE or TEA quantum efficiency and gas transmission [23].

    (b) The measurement of pad multiplicity per cluster as a function of cathode voltage for various photosensitive gases—effect of photon feedback [23].

    (c) The measurement of secondary photoelectron rate due to photon feedback per primary avalanche in the CRID detector [22] as a function of total

avalanche charge in C_2H_6 + TMAE gas for various TMAE bubbler temperatures and two different anode wire diameters.

13. The measurement of photon rate per avalanche electron for different quenchers at various partial pressures [21].

14. The results of the calculation of drift velocity (a) and single electron longitudinal diffusion (b) in helium-based gases [27] using a program WIRCHA [4].

15. Figure of merit fm_L (see text for definition) for longitudinal diffusion as a function of the reduced electric field for helium-based mixtures with 10% of quencher [28].

16. The measured effective ionization coefficient $\bar{\alpha}/N$ as a function of E/p in different gases [9].

17. A Monte Carlo simulation of the resolution in a 90% Ar + 10% CF_4 mixture at 1 atm in a 4 mm diameter straw tube [3]. The cross-hatched area represents the uncertainty in the attachment cross section.

18. The inverse mobility of positive ions as a function of the CH_4 fraction for gas mixtures of Ar + CH_4 or CF_4 + CH_4 [32].

19. (a) The experimental data on resolution obtained in 4 mm diameter straw tubes in 80% CF_4 + 20% C_4H_{10} gas [33].

    (b) A comparison of resolutions at the SSC rate and a slow rate.

20. Drift velocity in Xe + CF_4 (a) and Xe + CO_2 gas mixtures [10].

21. Fe^{55} pulse height spectra for 40% Xe + 60% CF_4 (1), 40% Xe + 40% CF_4 + 20% CH_4 (2) and 40% Xe + 40% CO_2 + 20% Ne (3) [10].

22. (a) A single gap parallel plate chamber (PPAC) with pad readout.

    (b) A wire chamber with pad readout.

23. (a) The TEA quantum efficiency as a function of photon wavelength with either helium (a) or CH_4 (b) as carrier gas [23]; curve (1) is from ref. 23 and curve (2) is from ref. 55.

(c) The TMAE quantum efficiency with helium carrier gas [23]; curve (1) is from ref. 23, curve (2) from ref. 55 and curve (3) from ref. 56.

(d) The quantum efficiency of CsI without and with adsorbed TMAE [23].

24. (a) Wire aging in CF_4 and 80% CF_4 + 20% iC_4H_{10} gases [7].

(b) Wire aging in 95% He + 5% C_2H_6 and 78% He + 15% CO_2 + 7% iC_4H_{10} gases [7].

(c) Average electron energy near the anode wire as calculated using Biagi's program [2,3].

25. Measurement of photon yield during avalanche in 90% Ar + 10% CH_4 gas either in self quenching streamer mode (a) or proportional mode (b) [51]; about 80% of CH and CH^+ fragments identified [52].

26. GC-MS analysis of avalanche products during aging test either in 50% Ar + 50% C_2H_6 gas (a,b) or CF_4 gas (c,d) [49,53,54].

Table 1. Number of primary electrons per 1 cm at 1 atm.

Gas	N_p (Rieke et al. [13])	N_p (Pansky et al. [12])
He	4.2	—
H_2	4.7	—
CH_4	25	26 (–2 +4%)
C_2H_6	41	51
C_3H_8	63	74
i-C_4H_{10}	84	93
DME	62	62
CF_4	51	—
TEA	—	144
TMAE	—	281

Table 2.

Helium

Disadvantages

1. Low primary ionization (4.2 prim. pairs/cm in pure helium).
2. Low drift velocity (<1 cm/μs in pure helium).
3. Large single electron diffusion [580 μm/sq(cm) in pure helium].
4. Possibility of secondary effects at small concentration of a quenching gas.

Advantages

1. Large radiation length (5284 m).
   => Low multiple scattering (below 1 GeV/c).
2. Small photon absorption cross section.
   => Low synchrotron radiation background.
3. Small Lorentz angle.
4. Allows low voltages on parallel plate chambers.
5. A good UV transparency (Cherenkov detectors).

CF_4

Disadvantages

1. Dissociative electron attachment.
2. Poor pulse height resolution in some mixtures.
3. By itself, it undergoes a wire aging.

Advantages

1. Very high electron drift velocity (>10 cm/μs).
2. Low diffusion (near thermal up to 2 kV/cm/atm).
3. High primary ionization (51 prim. pairs/cm).
4. In some admixtures, no wire aging observed.
5. In some admixtures, wire aging deposits etched away.
6. A good UV transparency (Cherenkov detectors).

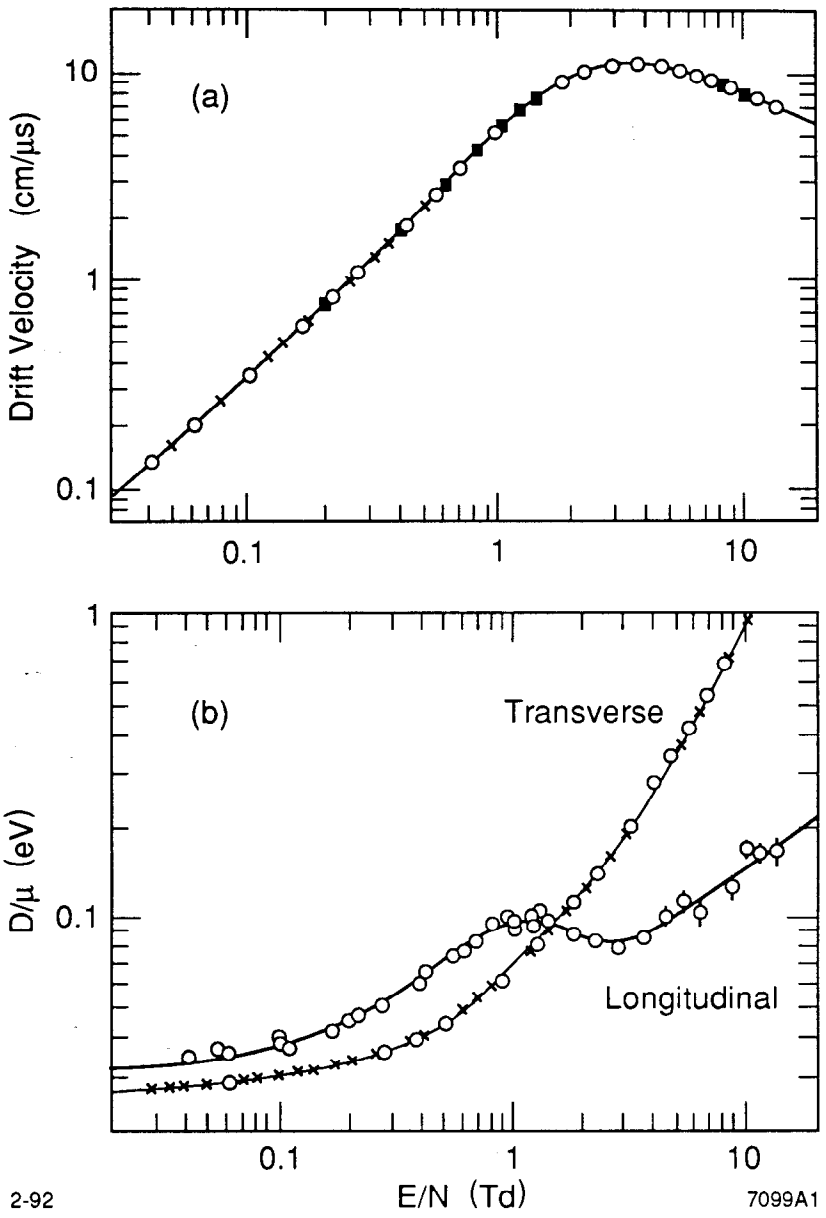
(a)
Drift Velocity (cm/μs)
10
1
0.1
0.1
1
10
(b)
Transverse
Longitudinal
D/μ (eV)
1
0.1
0.1
1
10
E/N (Td)
2-92
7099A1

Fig. 1

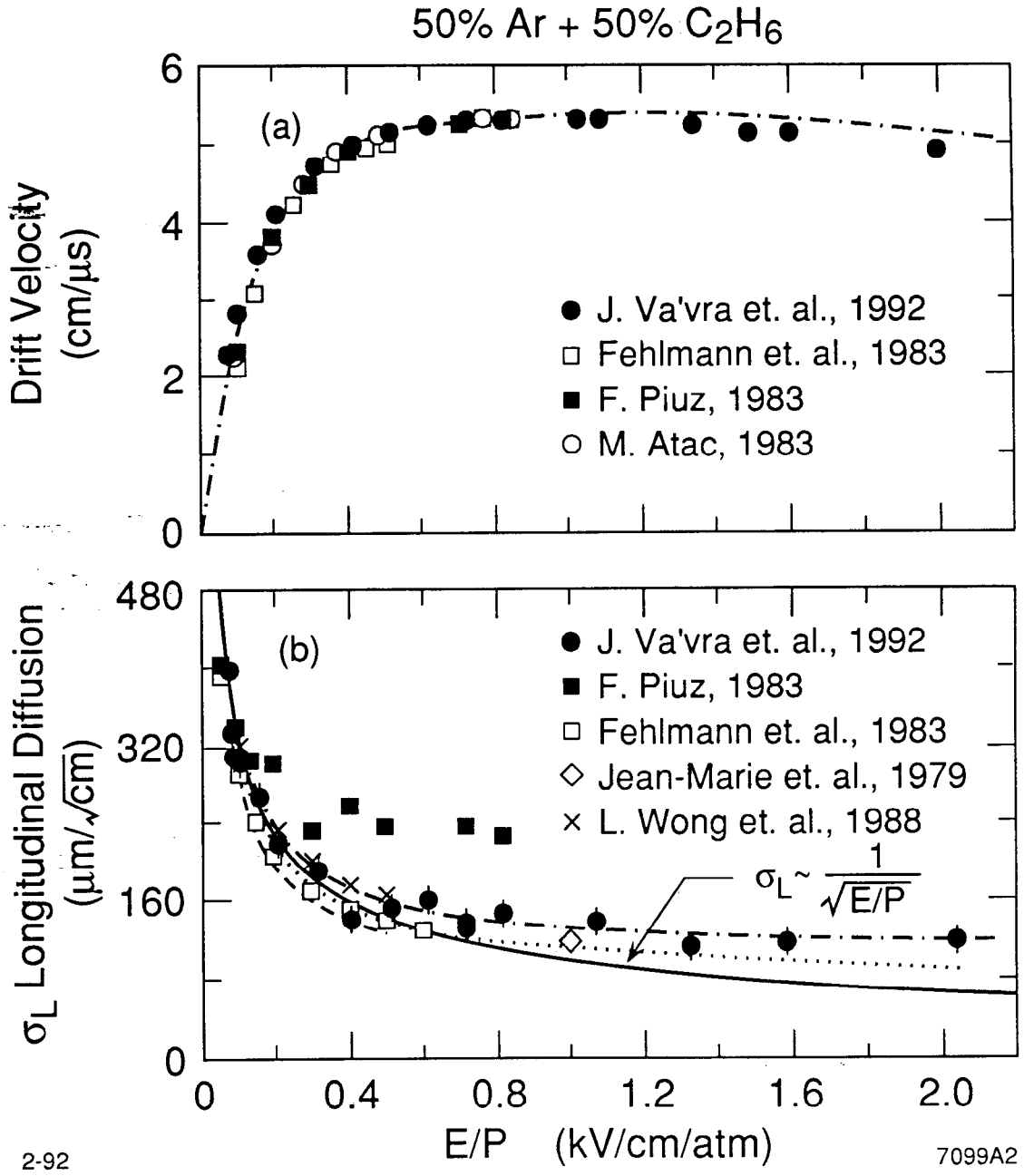
50% Ar + 50% C_2H_6
(a)
Drift Velocity (cm/μs)
6
4
2
0
J. Va'vra et. al., 1992
Fehlmann et. al., 1983
F. Piuz, 1983
M. Atac, 1983
(b)
σ_L Longitudinal Diffusion (μm/√cm)
480
320
160
0
J. Va'vra et. al., 1992
F. Piuz, 1983
Fehlmann et. al., 1983
Jean-Marie et. al., 1979
L. Wong et. al., 1988
$\sigma_L \sim \frac{1}{\sqrt{E/P}}$
0
0.4
0.8
1.2
1.6
2.0
E/P (kV/cm/atm)
2-92
7099A2

Fig. 2

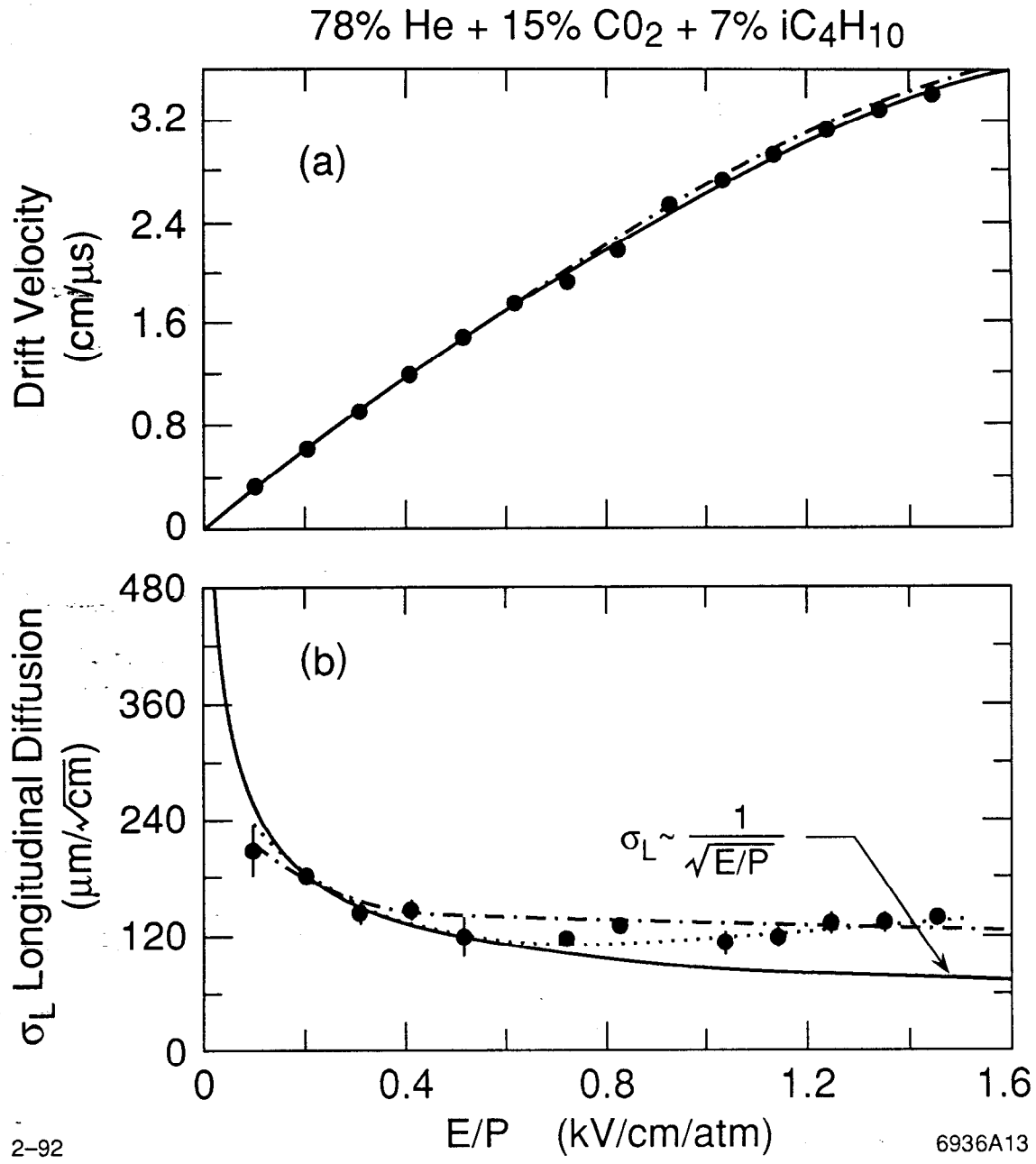
78% He + 15% $C0_2$ + 7% iC_4H_{10}
(a)
Drift Velocity (cm/μs)
3.2
2.4
1.6
0.8
0
(b)
σ_L Longitudinal Diffusion (μm/√cm)
480
360
240
120
0
$\sigma_L \sim \frac{1}{\sqrt{E/P}}$
0
0.4
0.8
1.2
1.6
E/P (kV/cm/atm)
2–92
6936A13

Fig. 3

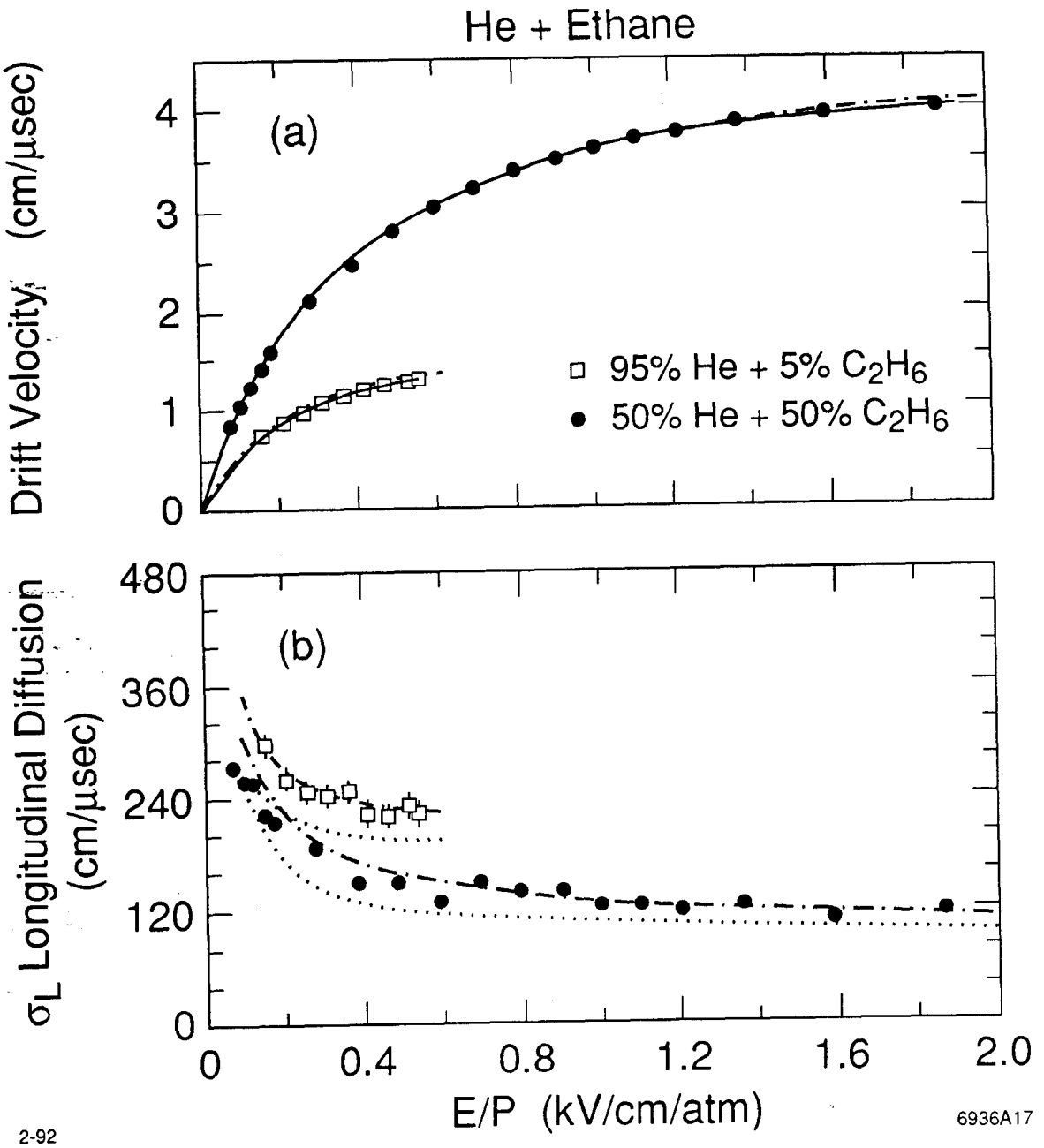
He + Ethane
(a)
Drift Velocity (cm/μsec)
4
3
2
1
0
95% He + 5% C_2H_6
50% He + 50% C_2H_6
(b)
σ_L Longitudinal Diffusion (cm/μsec)
480
360
240
120
0
0
0.4
0.8
1.2
1.6
2.0
E/P (kV/cm/atm)
2-92
6936A17

Fig. 4

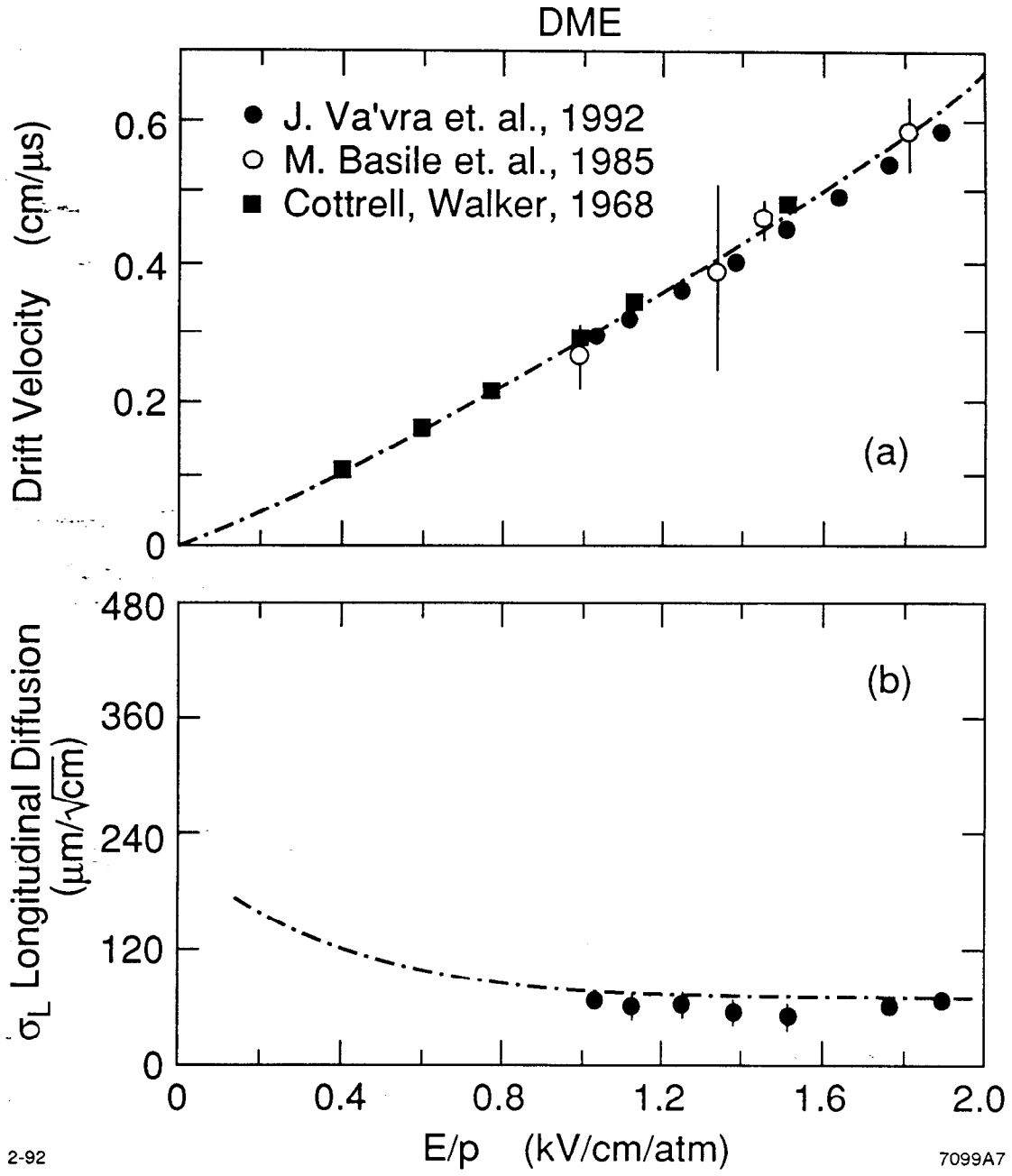
DME
J. Va'vra et. al., 1992
M. Basile et. al., 1985
Cottrell, Walker, 1968
Drift Velocity (cm/μs)
0.6
0.4
0.2
0
(a)
480
360
240
120
0
(b)
σL Longitudinal Diffusion (μm/√cm)
0
0.4
0.8
1.2
1.6
2.0
E/p (kV/cm/atm)
2-92
7099A7

Fig. 5

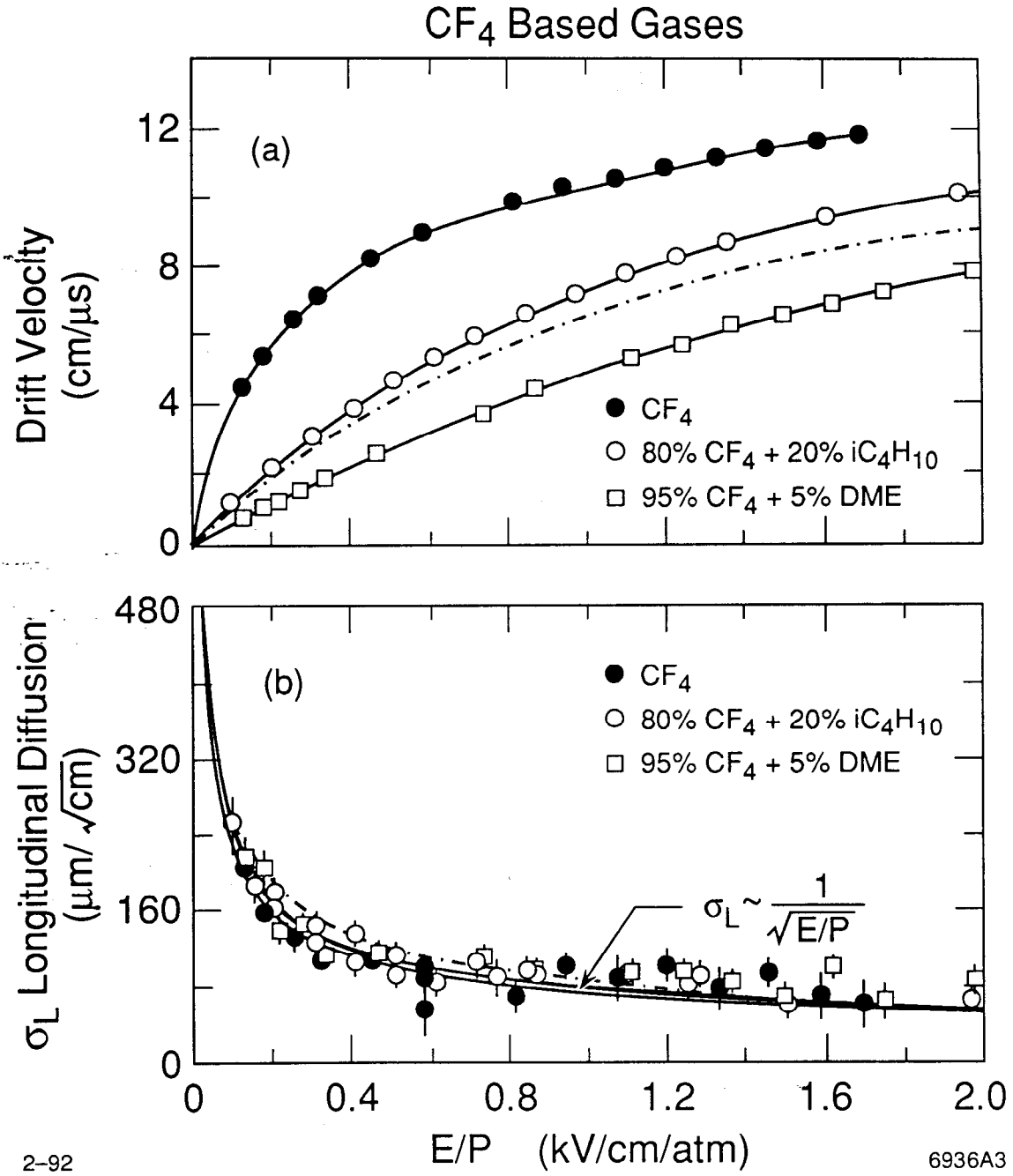
CF4 Based Gases
(a)
Drift Velocity (cm/μs)
12
8
4
0
CF4
80% CF4 + 20% iC4H10
95% CF4 + 5% DME
(b)
σL Longitudinal Diffusion (μm/√cm)
480
320
160
0
σL ~ 1/√E/P
0
0.4
0.8
1.2
1.6
2.0
E/P (kV/cm/atm)
2-92
6936A3

Fig. 6

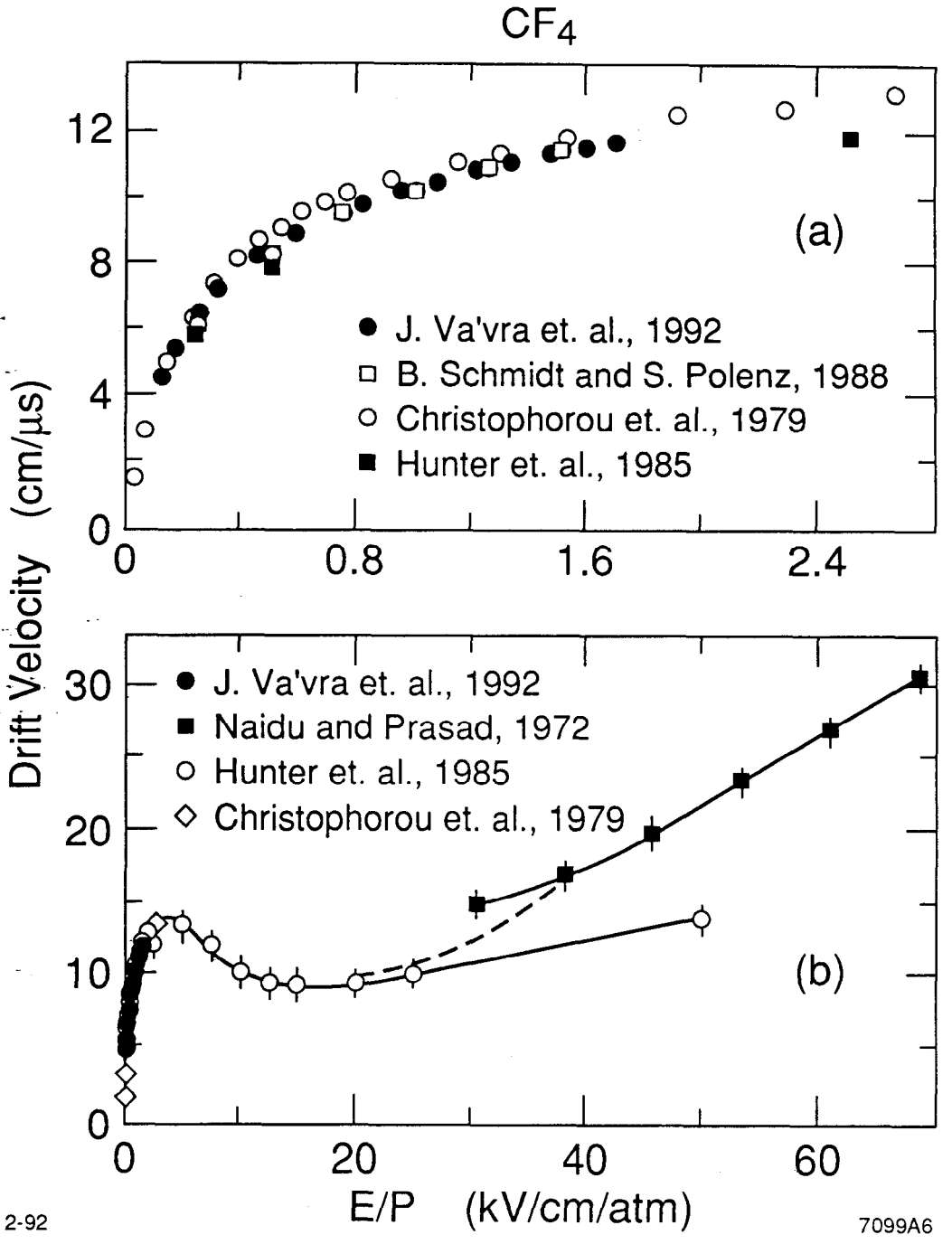
CF4
12
8
4
0
0
0.8
1.6
2.4
(a)
J. Va'vra et. al., 1992
B. Schmidt and S. Polenz, 1988
Christophorou et. al., 1979
Hunter et. al., 1985
Drift Velocity (cm/μs)
30
20
10
0
0
20
40
60
E/P (kV/cm/atm)
J. Va'vra et. al., 1992
Naidu and Prasad, 1972
Hunter et. al., 1985
Christophorou et. al., 1979
(b)
2-92
7099A6

Fig. 7

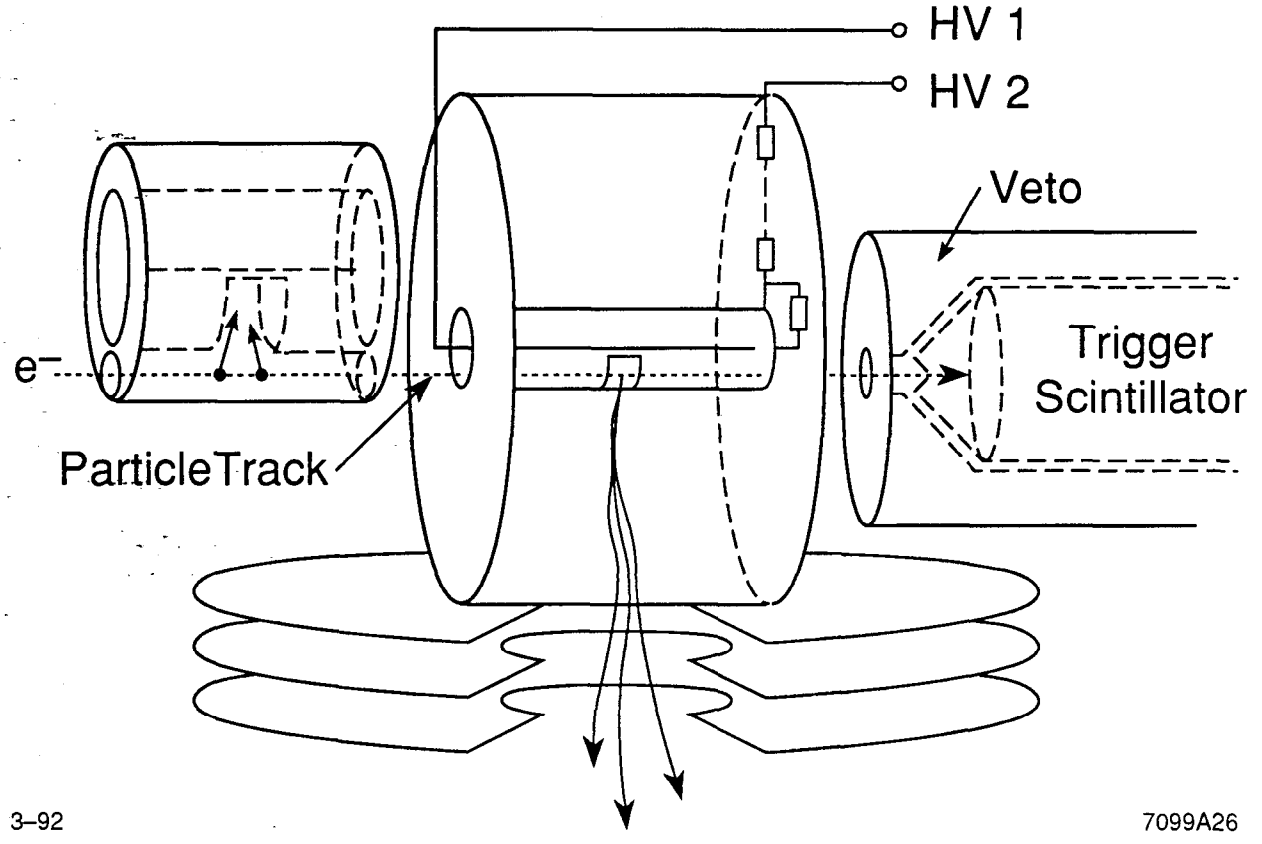
HV 1
HV 2
Veto
Trigger
Scintillator
e⁻
ParticleTrack
3–92
7099A26

Fig. 8

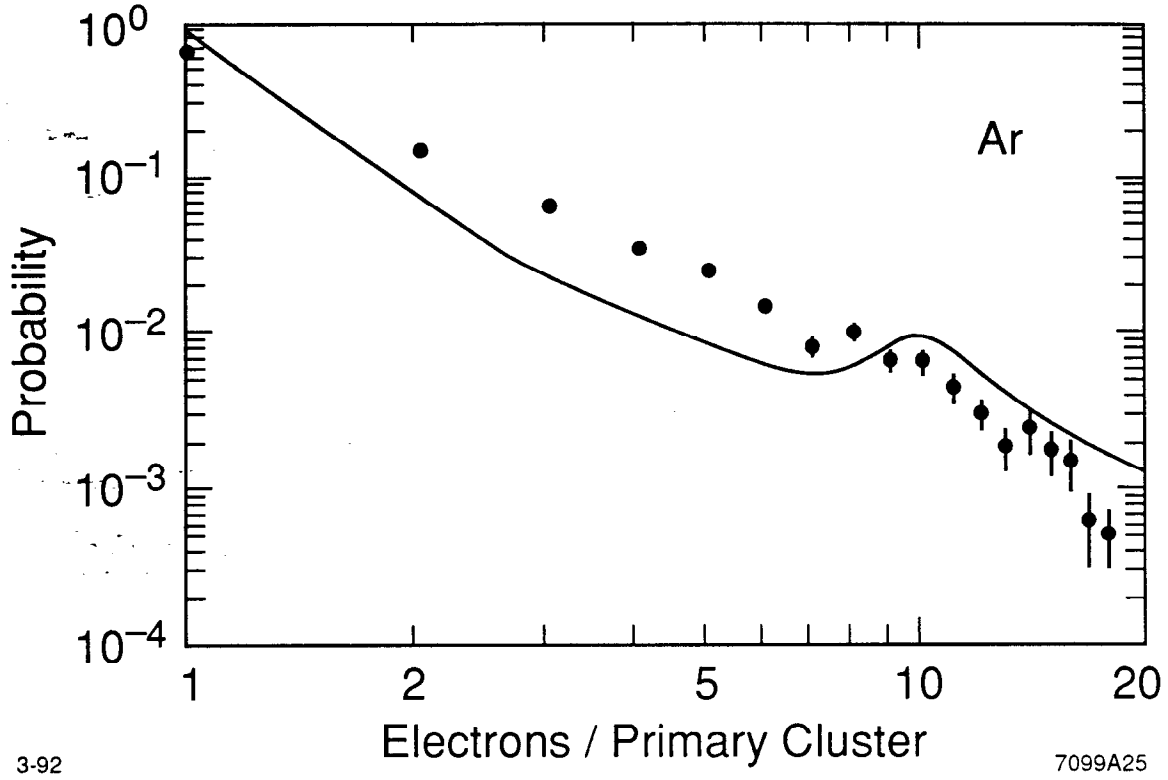
10^0
10^{-1}
10^{-2}
10^{-3}
10^{-4}
Probability
Ar
1
2
5
10
20
Electrons / Primary Cluster
3-92
7099A25

Fig. 9

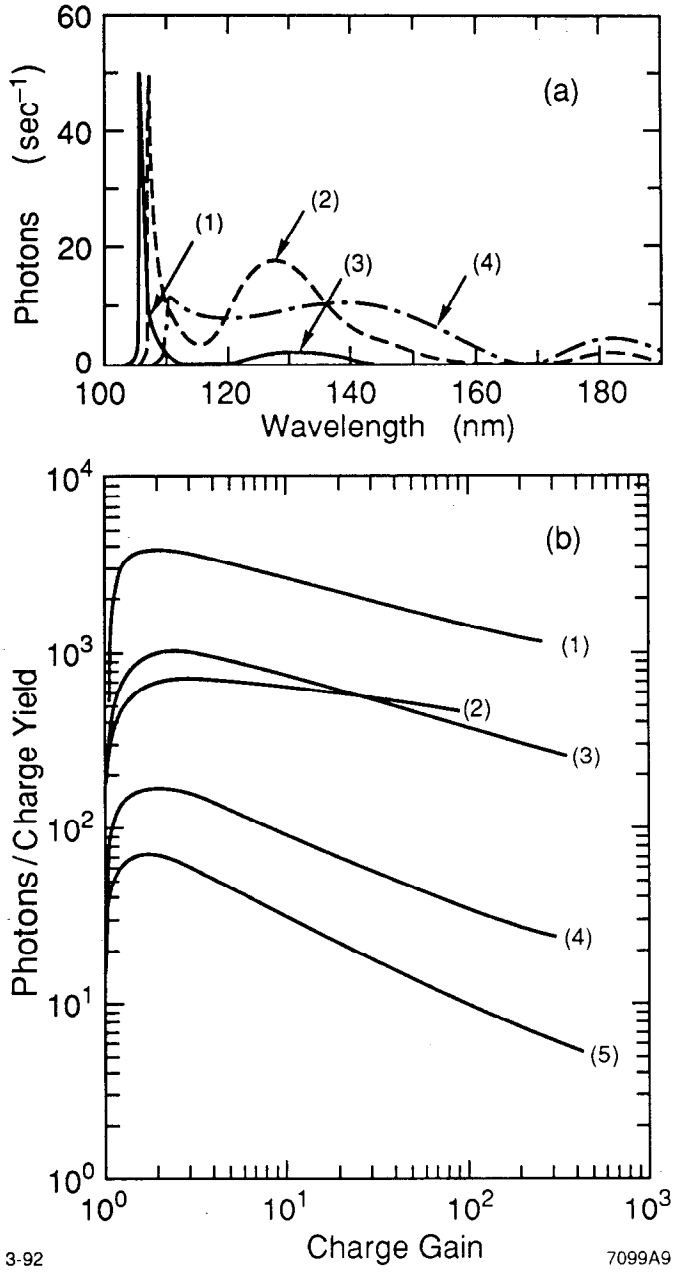
60
40
20
0
Photons (sec^{-1})
(a)
(1)
(2)
(3)
(4)
100
120
140
160
180
Wavelength (nm)
10^4
10^3
10^2
10^1
10^0
Photons / Charge Yield
(b)
(1)
(2)
(3)
(4)
(5)
10^0
10^1
10^2
10^3
Charge Gain
3-92
7099A9

Fig. 10

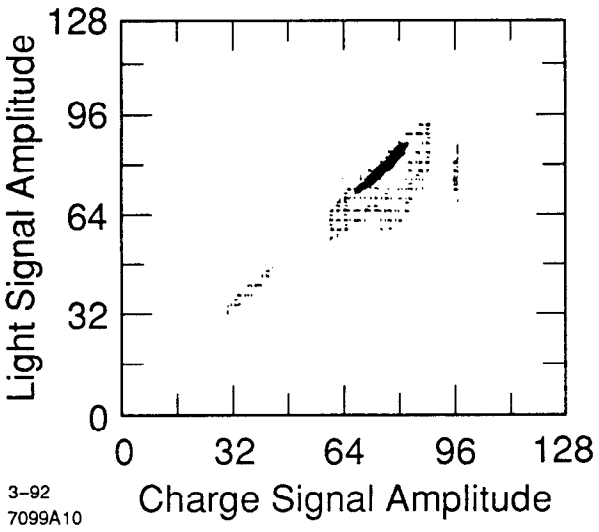
Light Signal Amplitude
128
96
64
32
0
0
32
64
96
128
Charge Signal Amplitude
3-92
7099A10

Fig. 11

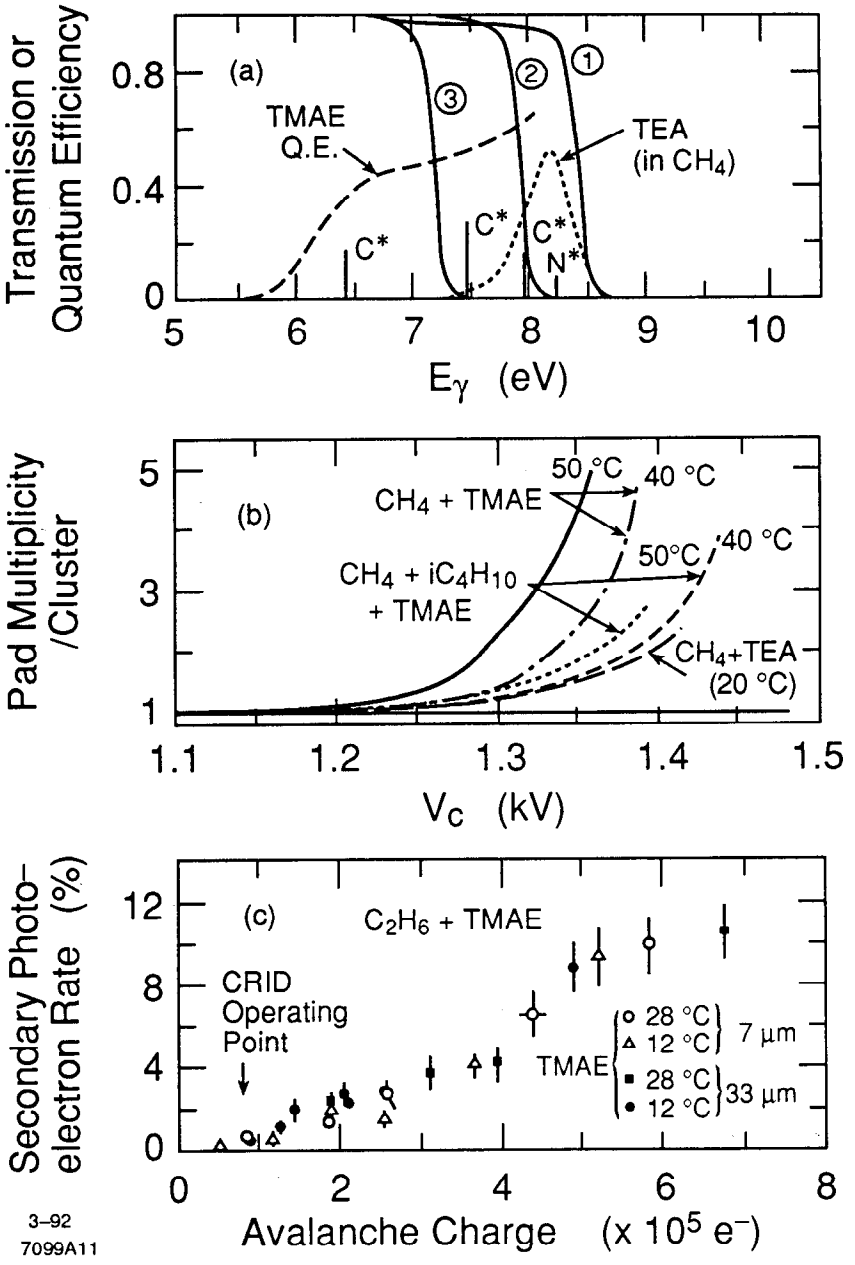
Transmission or Quantum Efficiency
(a)
TMAE Q.E.
TEA (in CH4)
C*
C*
C*
N*
①
②
③
0.8
0.4
0
5
6
7
8
9
10
Eγ (eV)
Pad Multiplicity /Cluster
(b)
CH4 + TMAE
50 °C
40 °C
CH4 + iC4H10 + TMAE
50°C
40 °C
CH4+TEA (20 °C)
5
3
1
1.1
1.2
1.3
1.4
1.5
Vc (kV)
Secondary Photo-electron Rate (%)
(c)
C2H6 + TMAE
CRID Operating Point
TMAE
28 °C
12 °C
7 µm
28 °C
12 °C
33 µm
12
8
4
0
0
2
4
6
8
Avalanche Charge (x 10^5 e^-)
3-92
7099A11

Fig. 12

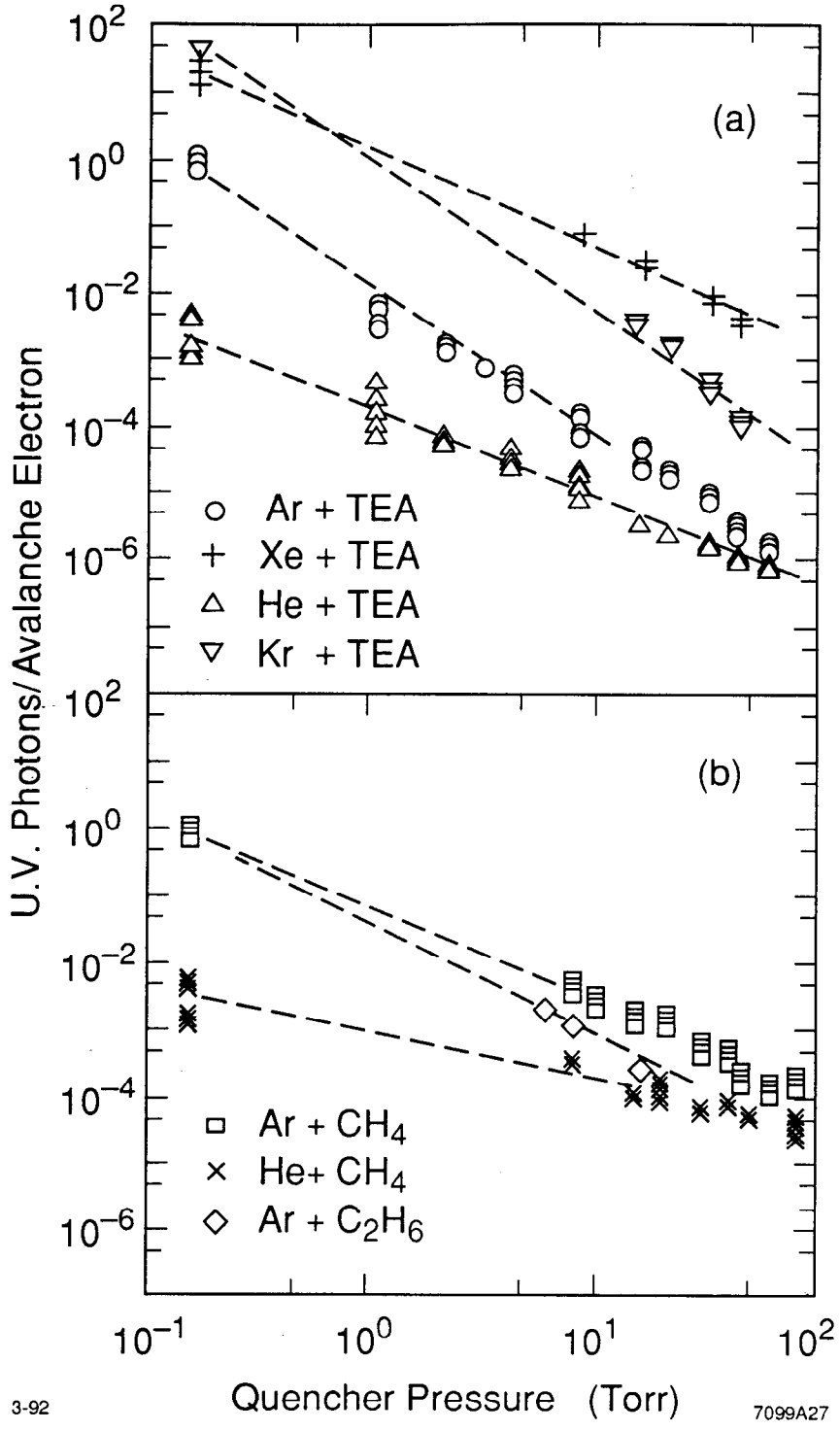
(a)
(b)
Ar + TEA
Xe + TEA
He + TEA
Kr + TEA
Ar + CH_4
He+ CH_4
Ar + C_2H_6
U.V. Photons/Avalanche Electron
Quencher Pressure (Torr)
3-92
7099A27

Fig. 13

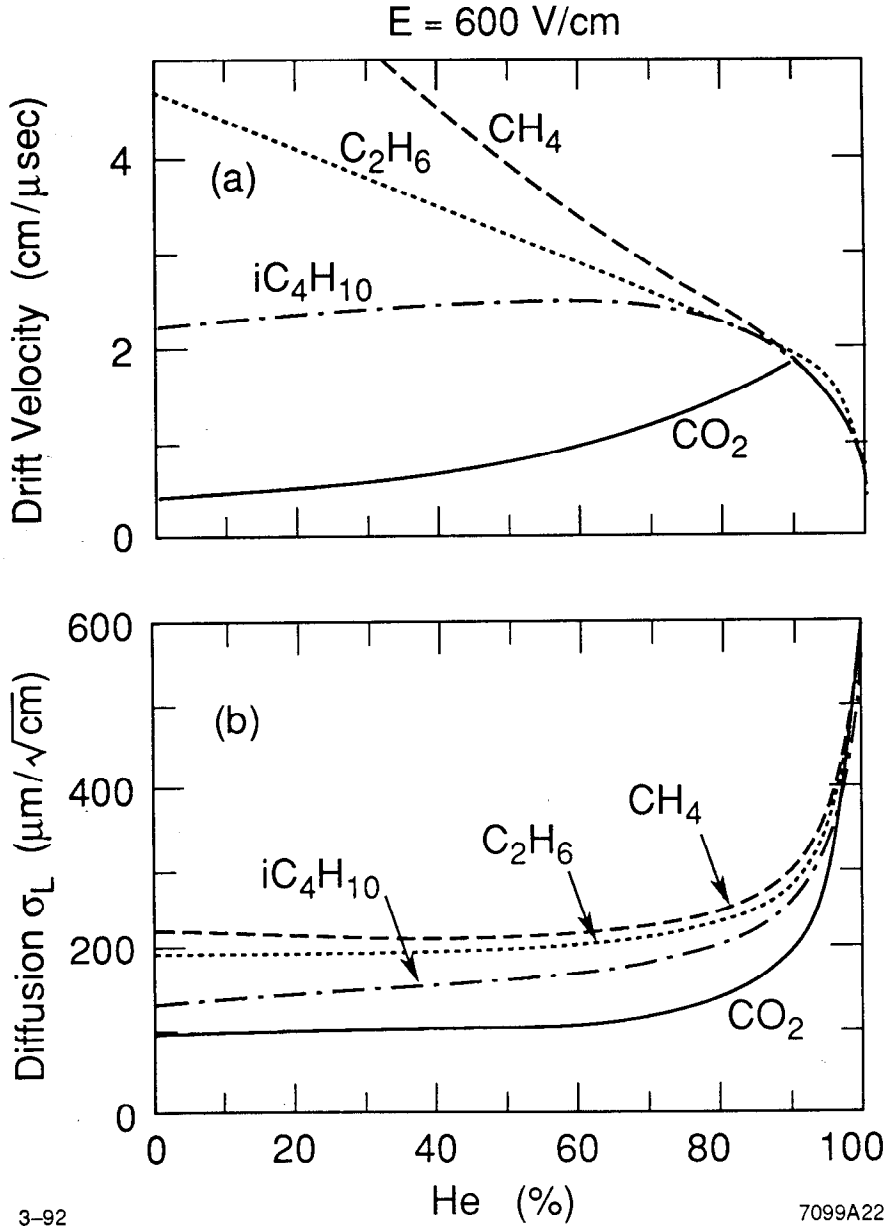
E = 600 V/cm
Drift Velocity (cm/μsec)
4
2
0
(a)
CH4
C2H6
iC4H10
CO2
Diffusion σL (μm/√cm)
600
400
200
0
(b)
CH4
C2H6
iC4H10
CO2
0
20
40
60
80
100
He (%)
3-92
7099A22

Fig. 14

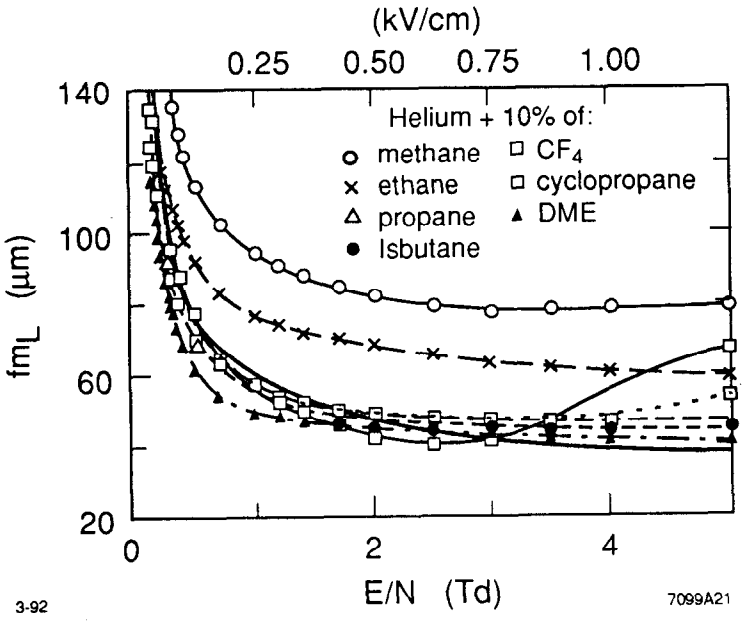
(kV/cm)
0.25
0.50
0.75
1.00
140
100
60
20
0
2
4
fm_L (μm)
E/N (Td)
Helium + 10% of:
methane
ethane
propane
Isbutane
CF_4
cyclopropane
DME
3-92
7099A21

Fig. 15

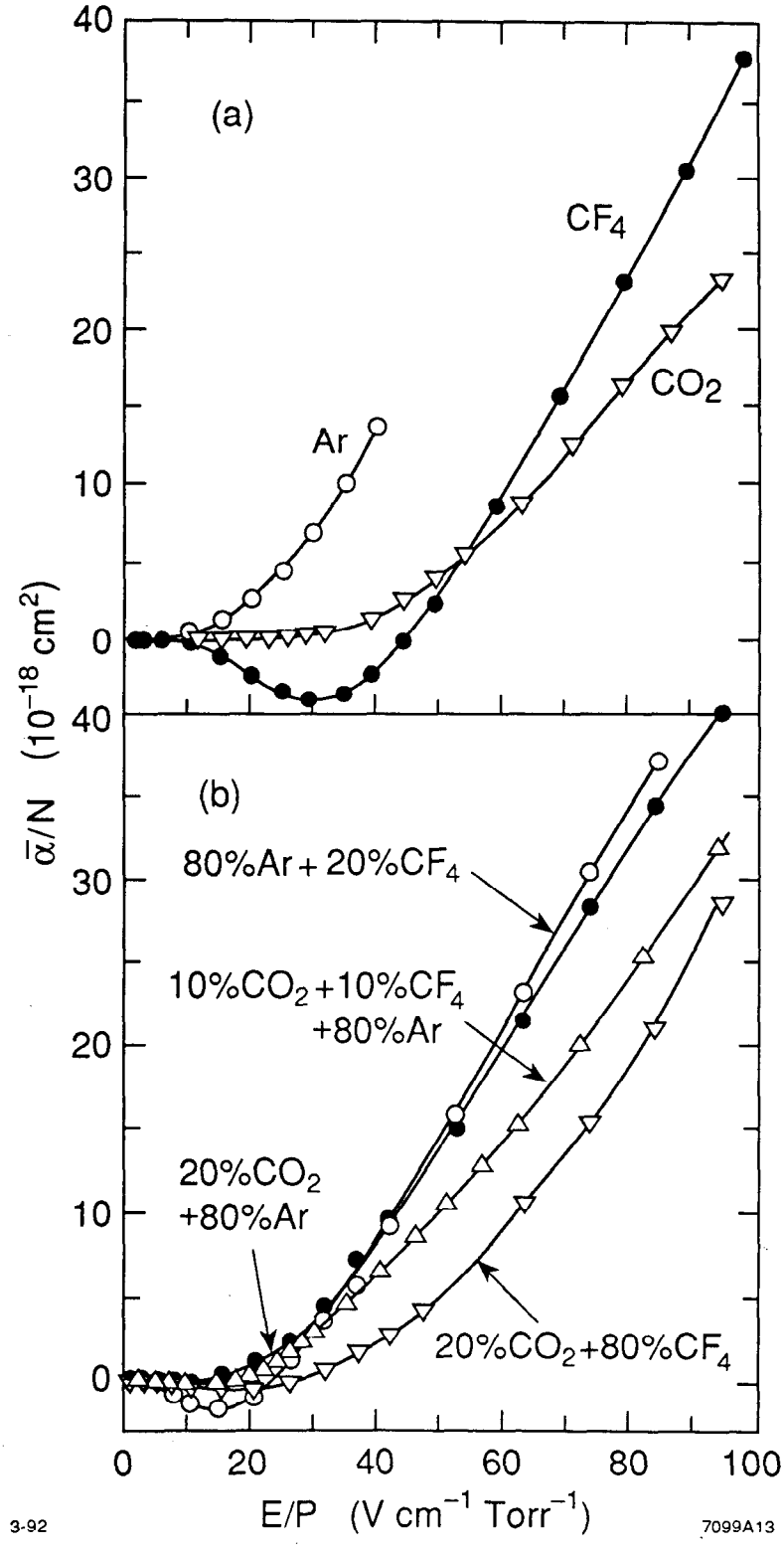
(a)
CF4
CO2
Ar
(b)
80%Ar + 20%CF4
10%CO2 + 10%CF4
+80%Ar
20%CO2
+80%Ar
20%CO2+80%CF4
ᾱ/N (10^-18 cm^2)
E/P (V cm^-1 Torr^-1)
0
10
20
30
40
0
20
40
60
80
100
3-92
7099A13

Fig. 16

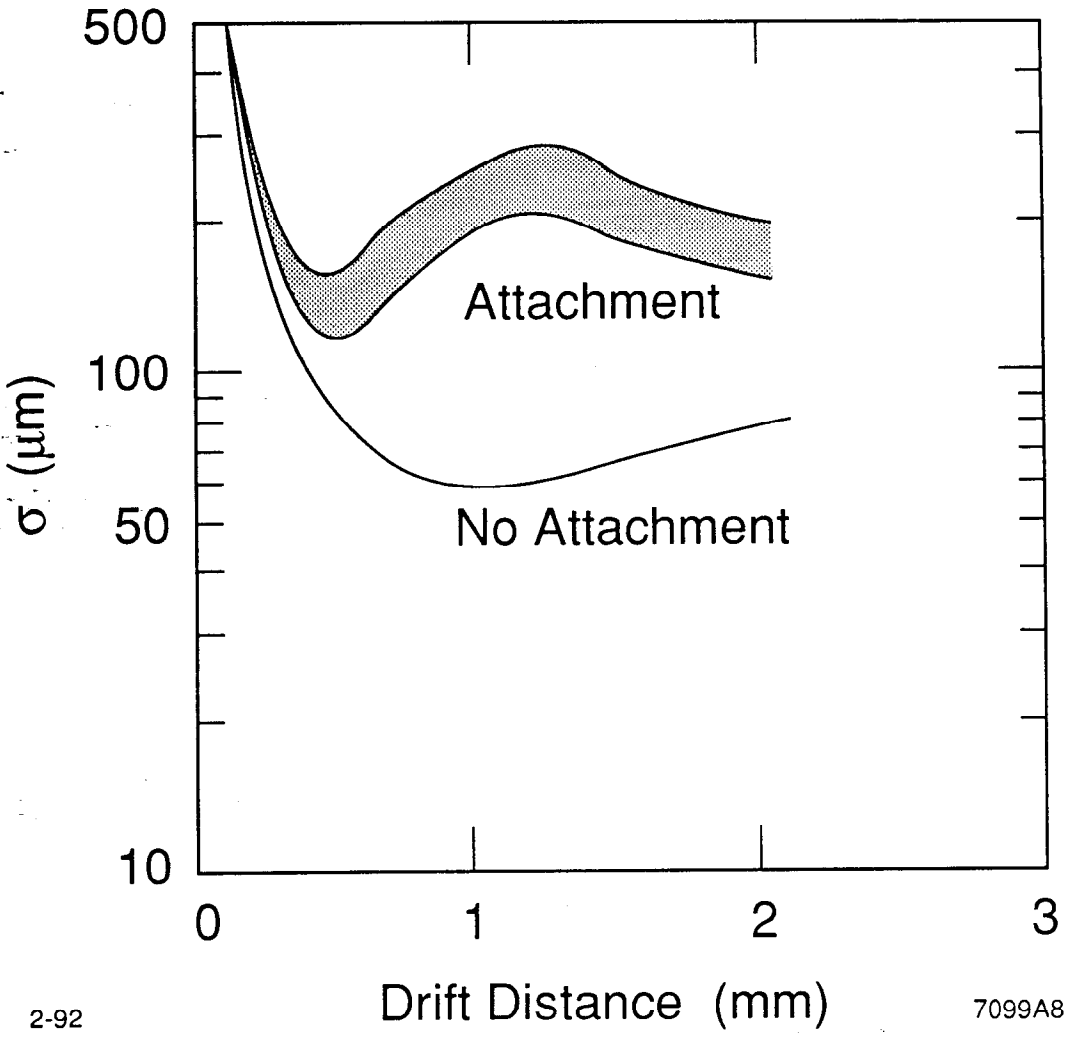
500
100
50
10
σ (μm)
Attachment
No Attachment
0
1
2
3
Drift Distance (mm)
2-92
7099A8

Fig. 17

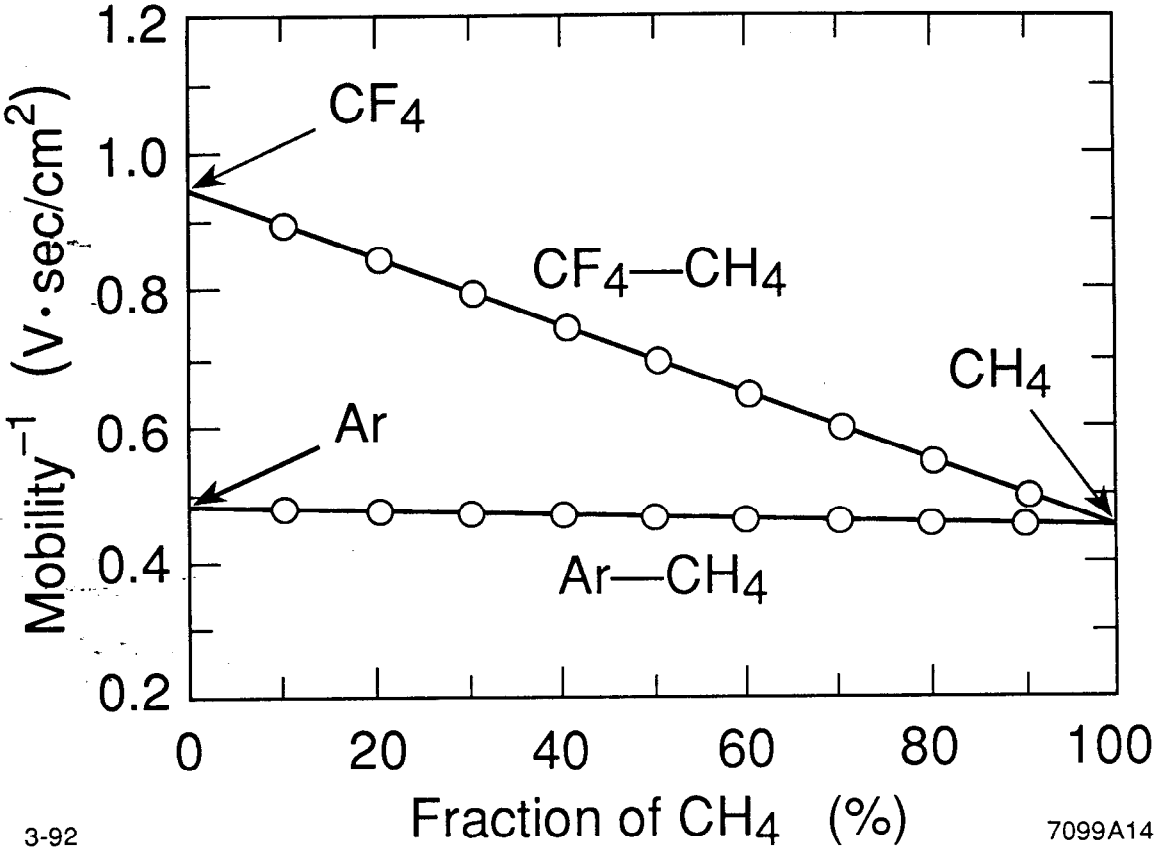
1.2
1.0
0.8
0.6
0.4
0.2
Mobility^{-1} (V·sec/cm^2)
CF_4
CF_4—CH_4
CH_4
Ar
Ar—CH_4
0
20
40
60
80
100
Fraction of CH_4 (%)
3-92
7099A14

Fig. 18

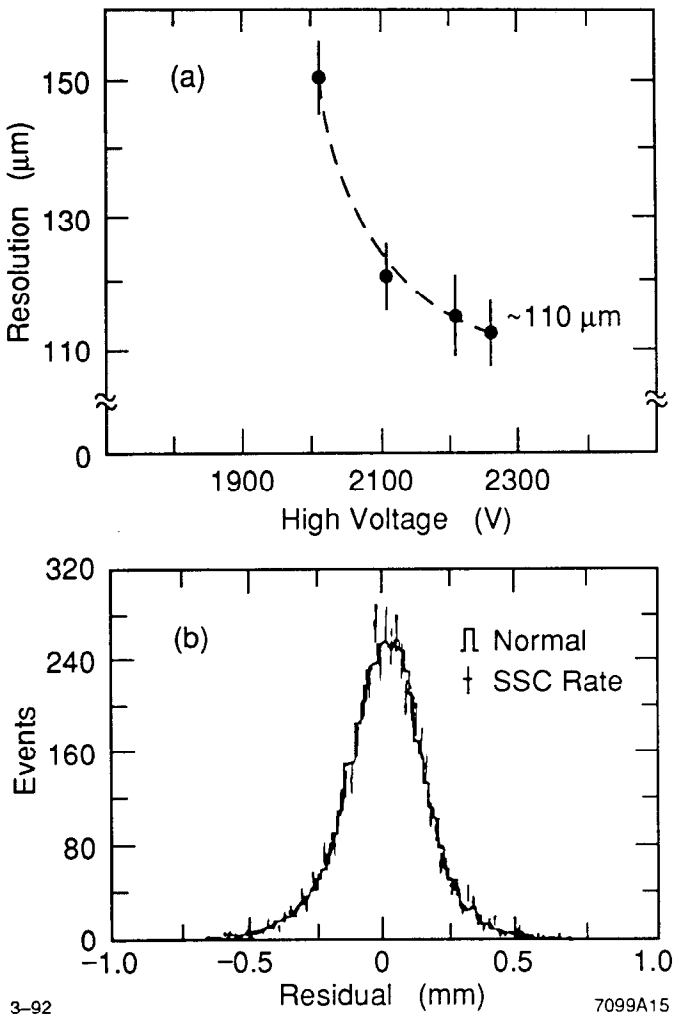
(a)
150
130
110
0
Resolution (μm)
~110 μm
1900
2100
2300
High Voltage (V)
(b)
Normal
SSC Rate
320
240
160
80
0
Events
−1.0
−0.5
0
0.5
1.0
Residual (mm)
3–92
7099A15

Fig. 19

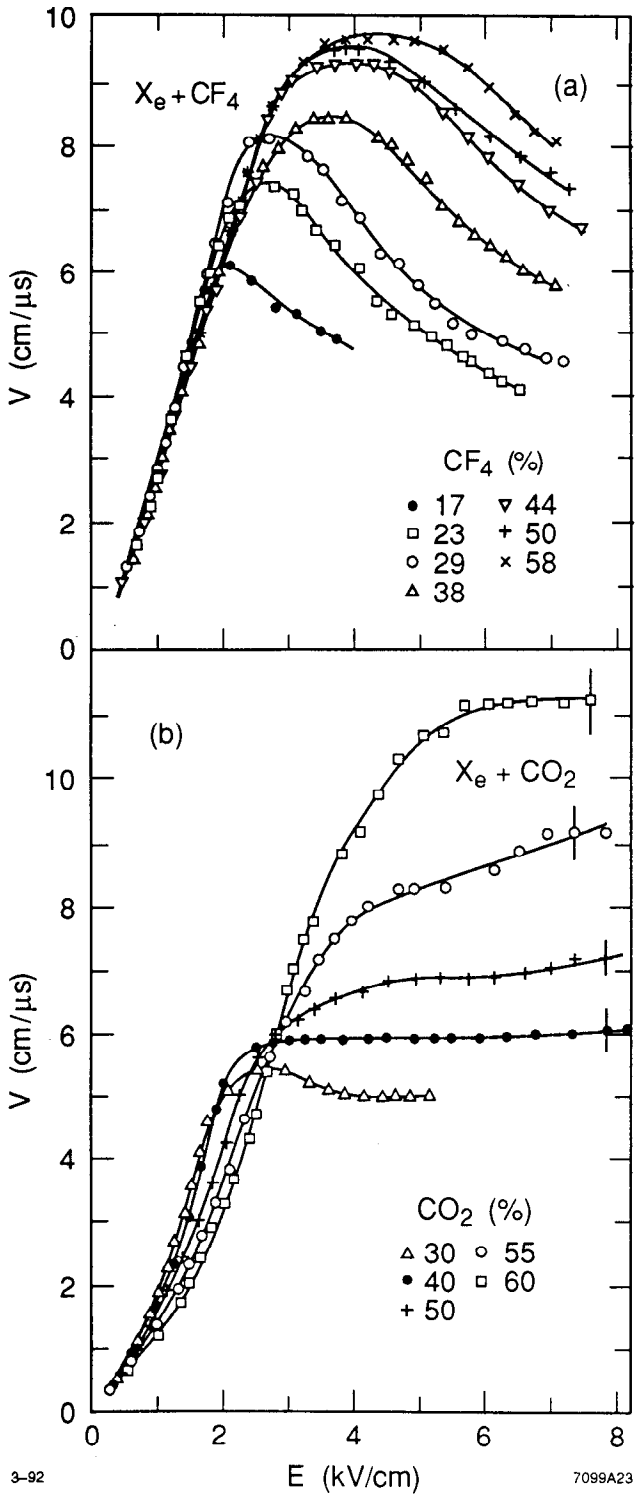
10
8
6
4
2
0
V (cm/μs)
$X_e + CF_4$
(a)
CF_4 (%)
• 17
▽ 44
□ 23
+ 50
○ 29
× 58
△ 38
(b)
$X_e + CO_2$
CO_2 (%)
△ 30
○ 55
• 40
□ 60
+ 50
0
2
4
6
8
E (kV/cm)
3-92
7099A23

Fig. 20

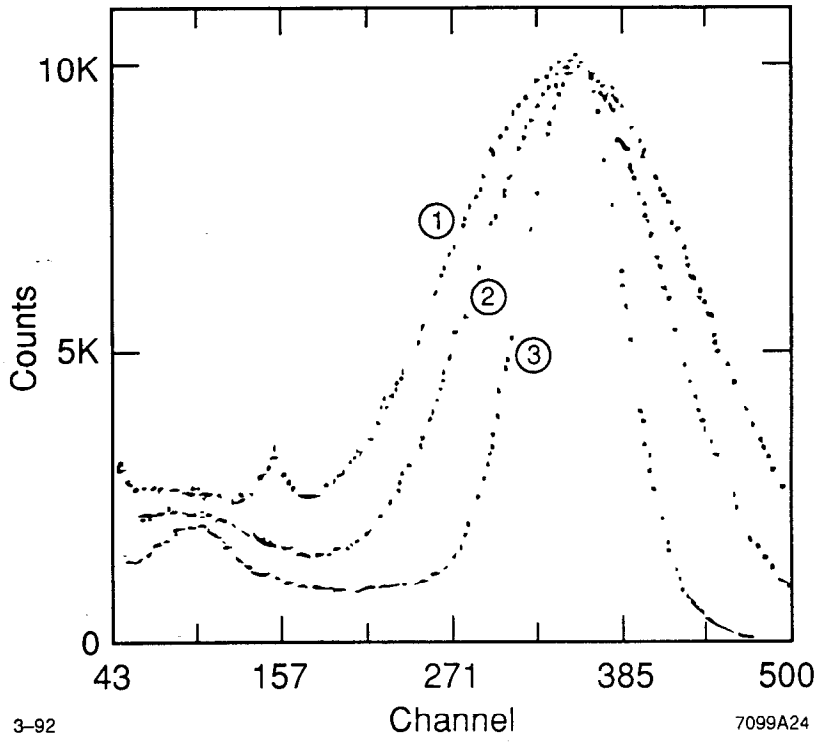

Fig. 21

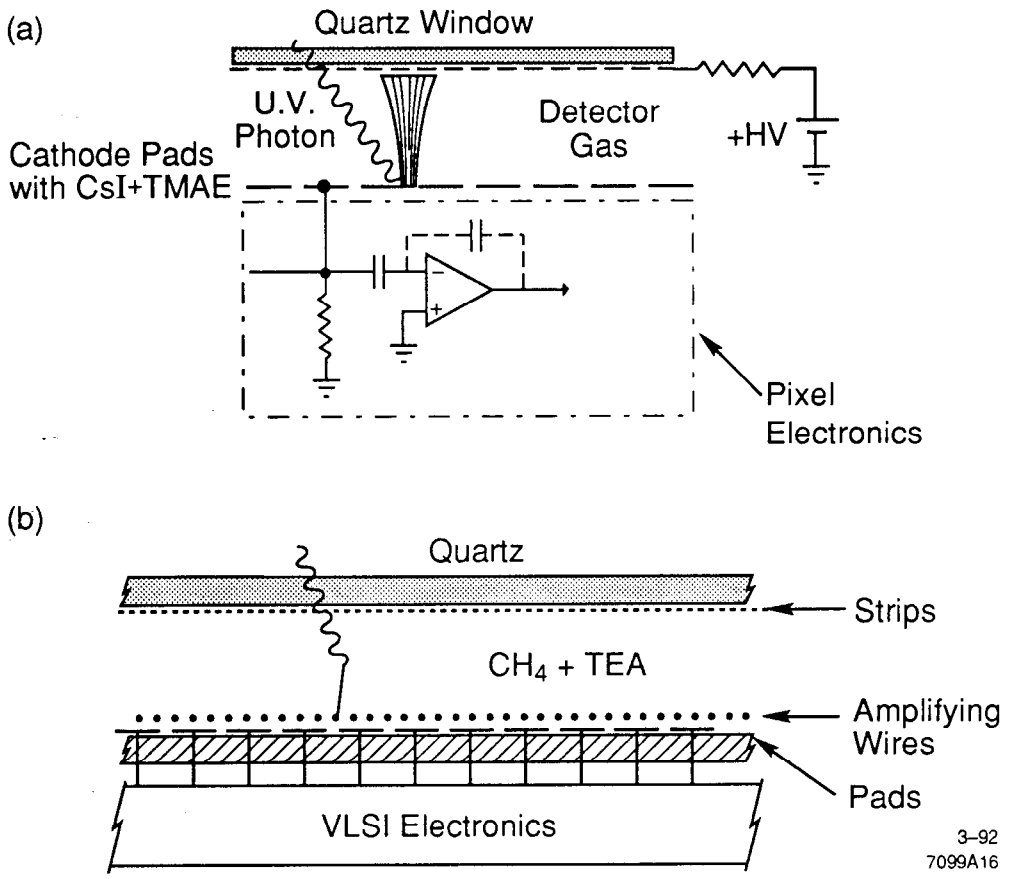
(a)
Quartz Window
U.V.
Photon
Detector
Gas
+HV
Cathode Pads
with CsI+TMAE
Pixel
Electronics
(b)
Quartz
Strips
CH_4 + TEA
Amplifying
Wires
Pads
VLSI Electronics
3-92
7099A16

Fig. 22

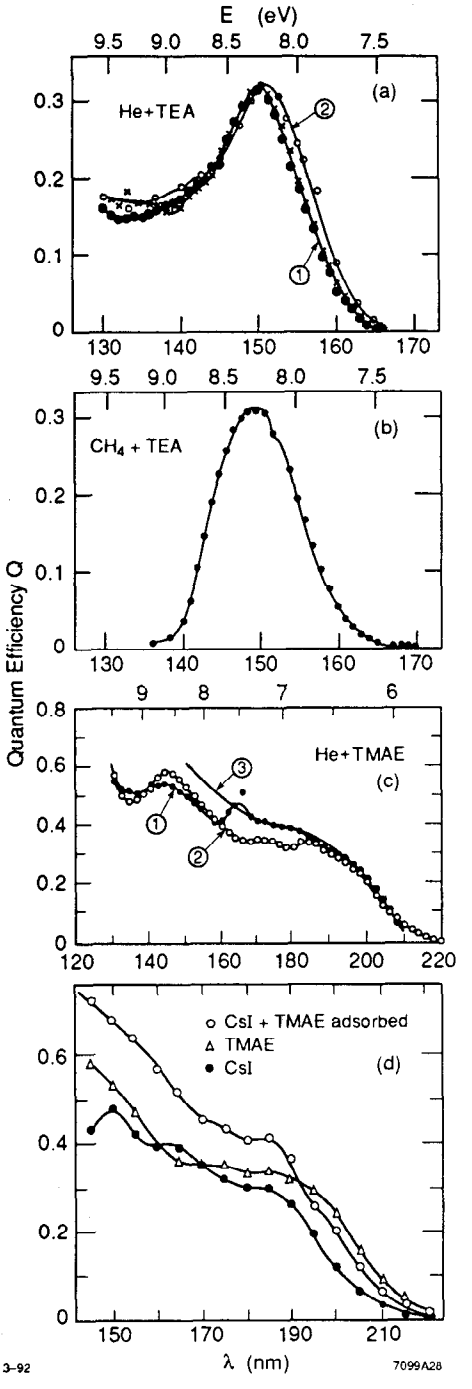
E (eV)
9.5 9.0 8.5 8.0 7.5
He+TEA
(a)
CH4 + TEA
(b)
Quantum Efficiency Q
9 8 7 6
He+TMAE
(c)
CsI + TMAE adsorbed
TMAE
CsI
(d)
λ (nm)
3-92
7099A28

Fig. 23

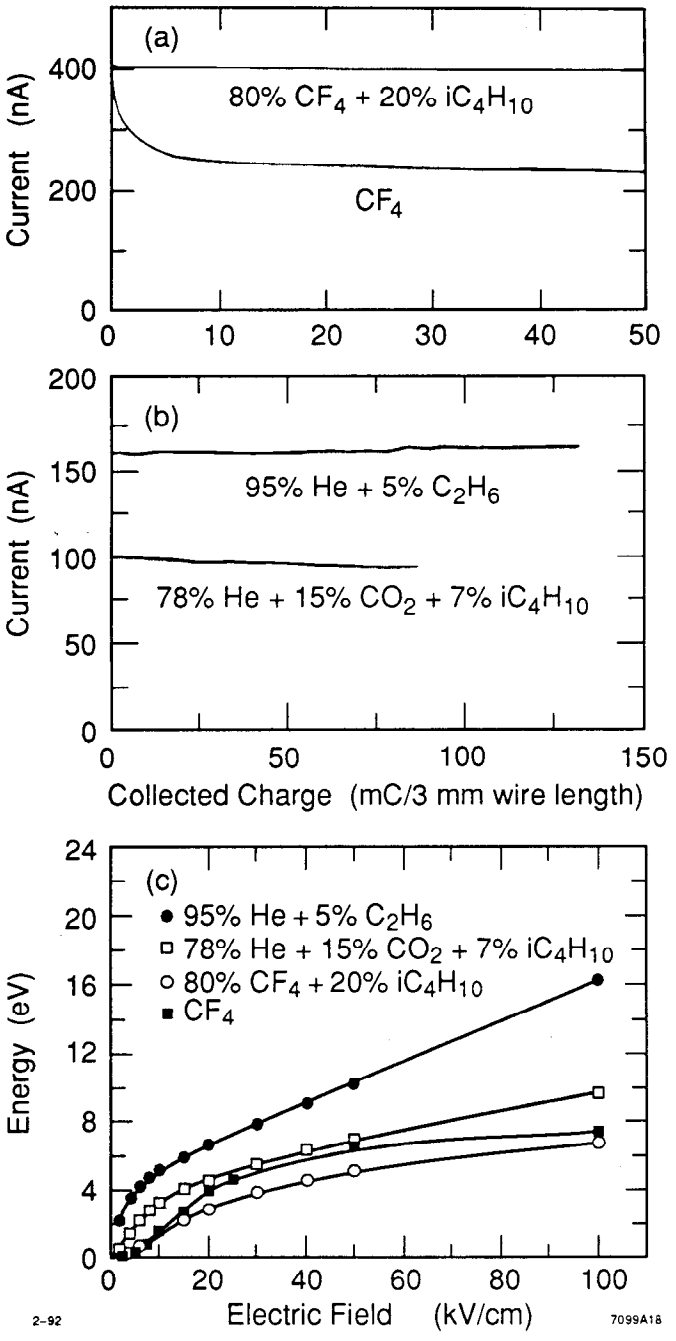
(a)
80% CF_4 + 20% iC_4H_{10}
CF_4
Current (nA)
400
200
0
0
10
20
30
40
50
(b)
95% He + 5% C_2H_6
78% He + 15% CO_2 + 7% iC_4H_{10}
Current (nA)
200
150
100
50
0
0
50
100
150
Collected Charge (mC/3 mm wire length)
(c)
95% He + 5% C_2H_6
78% He + 15% CO_2 + 7% iC_4H_{10}
80% CF_4 + 20% iC_4H_{10}
CF_4
Energy (eV)
24
20
16
12
8
4
0
0
20
40
60
80
100
Electric Field (kV/cm)
2-92
7099A18

Fig. 24

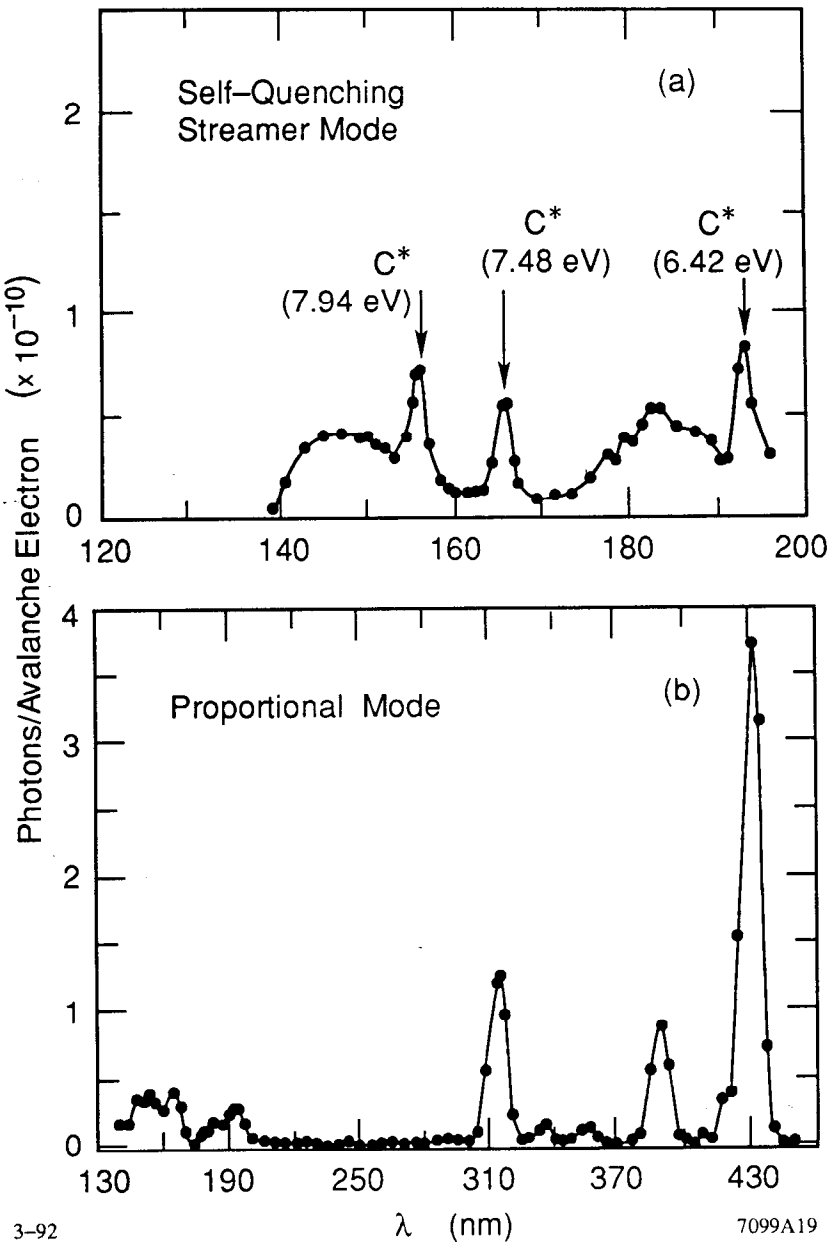
Self–Quenching
Streamer Mode
(a)
C*
(7.94 eV)
C*
(7.48 eV)
C*
(6.42 eV)
Photons/Avalanche Electron (x 10⁻¹⁰)
0
1
2
120
140
160
180
200
Proportional Mode
(b)
0
1
2
3
4
130
190
250
310
370
430
λ (nm)
3–92
7099A19

Fig. 25

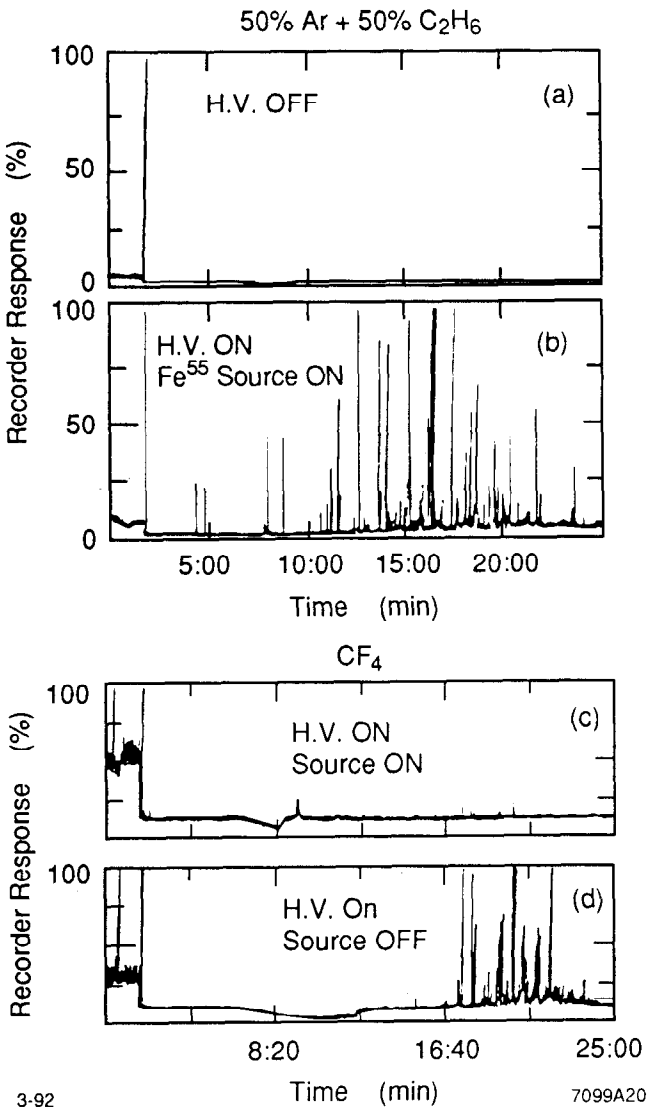
50% Ar + 50% C_2H_6
100
50
0
H.V. OFF
(a)
Recorder Response (%)
100
50
0
H.V. ON
Fe^{55} Source ON
(b)
5:00
10:00
15:00
20:00
Time (min)
CF_4
100
H.V. ON
Source ON
(c)
Recorder Response (%)
100
H.V. On
Source OFF
(d)
8:20
16:40
25:00
Time (min)
3-92
7099A20

Fig. 26